**Title:**

# Cellular heterogeneity in pressure and growth emerges from tissue topology and geometry

Yuchen Long[1,*], Ibrahim Cheddadi[2,4], Vincent Mirabet[1], Gabriella Mosca[3], Mathilde Dumond[1,5], Jan Traas[1], Christophe Godin[1,2], Arezki Boudaoud[1,*].

1. Laboratoire Reproduction et Développement des Plantes, Université de Lyon, ENS de Lyon, UCB Lyon 1, CNRS, INRA, INRIA, F-69342, Lyon, France.

2. INRIA/CIRAD/INRA Project-team Virtual Plants, France.

3. Department of Plant and Microbial Biology, University of Zürich, Zollikerstrasse 107, CH-8008 Zürich, Switzerland.

4. Current address: Univ. Grenoble Alpes, CNRS, Grenoble INP, TIMC-IMAG, 38000 Grenoble, France.

5. Current address: Department of Biosystems Science and Engineering, ETH Zurich, Mattenstrasse 26, 4058, Basel, Switzerland.

*. Correspondence and requests for materials should be addressed to yuchen.long@ens-lyon.fr or arezki.boudaoud@ens-lyon.fr

The authors declare no competing financial interests.

**Summary**

Cell-to-cell heterogeneity prevails in many biological systems, although its origin and function are often unclear. Cell hydrostatic pressure, alias turgor pressure, is essential in physiology and morphogenesis, and its spatial variations are often overlooked. Here, based on a mathematical model describing cell mechanics and water movement in a plant tissue, we predict that cell pressure anticorrelates with cell neighbour number. Using atomic force microscopy, we confirm this prediction in the Arabidopsis shoot apical meristem, a population of stem cells that generate all plant aerial organs. Pressure is predicted to correlate either positively or negatively with cellular growth rate depending on osmotic drive, cell wall extensibility, and hydraulic conductivity. The meristem exhibits one of these two regimes depending on conditions, suggesting that, in this tissue, water conductivity is non-negligible in growth control. Our results illustrate links between local topology, cell mechanical state and cell growth, with potential roles in tissue homeostasis.

**Key words**

Cellular heterogeneity, hydrostatic pressure, tissue topology, growth mechanics, tissue hydraulics, atomic force microscopy, biophysical modelling.

**Highlights**

- A mechano-hydraulic model of tissue growth predicts heterogeneity in cell pressure and in cell growth according to local tissue topology.
- Indentation-based measurement of cell pressure in the shoot apical meristem of *Arabidopsis thaliana*, together with a realistic mechanical model of tissue indentation, reveals pressure variations according to cell size and cell neighbour number.
- Cell growth in the Arabidopsis shoot apical meristem either correlates or anti-correlates with cell neighbour number, which can be retrieved by the model using experimentally-based parameters.

## Introduction

45    Cell-to-cell fluctuations are observed in many biological processes like gene expression,

47    signalling, cell size regulation and growth [1–8]. Notably, heterogeneity in cell size and growth

48    rate often prevails and may impact tissue patterning and macroscopic growth robustness [1,2].

49    Cell volume change is driven by osmosis [9–11] and the resulting intracellular hydrostatic

50    pressure, and is restrained by peripheral constraints — plasma membrane, cytoskeletal cortex,

51    extracellular matrix, or cell wall — in plant cells [12], animal cells [13] including tumorous

52    [14], and microbial cells [15] (Fig. 1a).

53    Due to high difference between internal and external osmotic potential, cells with rigid cell

54    walls – like in plants, bacteria and fungi – accumulate hydrostatic pressure, alias turgor pressure,

55    often greater than atmospheric pressure (Fig. S1) [12]. Animal cells also accumulate hydrostatic

56    pressure, especially when compacted or contracting [13,14], though to a lesser extent than

57    walled cells. Whereas it is increasingly realized that pressure regulation is crucial for the general

58    physiology, growth and signalling in animal [9,11,13] and plant cells [16–19], pressure remains

59    poorly characterized in multicellular contexts.

60    In plants, turgor pressure drives cells expansion, which is classically modelled as visco-elasto-

61    plastic process: irreversible expansion occurs when the pressure exceeds a threshold value and

62    the cell deforms reversibly when pressure is smaller, as depicted in the Lockhart-Ortega

63    equation (Fig. 1b) [20]:

$$\frac{1}{V}\frac{\mathrm{d}V}{\mathrm{d}t} = \varphi(P - P^Y)_+ + \frac{1}{E^V}\frac{\mathrm{d}P}{\mathrm{d}t}$$

65    where $V$ is cell volume, $P$ is turgor pressure, $P^Y$ is the pressure threshold for irreversible

66    expansion, $\varphi$ is global wall extensibility (akin to inverse of viscosity) and $E^V$ is the cell

67    volumetric modulus, while the $_+$ index indicates that irreversible expansion occurs only if $P >$

68    $P^Y$. For single cell, turgor pressure positively correlates with total growth rate (Fig. 1b). Other

69    experimental observations in single-cell systems suggest that growth rate and pressure level are

70    not always associated [15,21], making it difficult to assess and understand the link between

71    growth regulation and cellular pressure build-up.

72  In multicellular context, like the plant shoot apex and sepal epidermis, neighbouring cells grow

73  at notably different rates [1]. This prompts the question, according to the Lockhart-Ortega

74  equation, of whether turgor pressure also varies between neighbouring plant cells. Intuitively,

75  pressure difference should be equalized by plasmodesmata, symplasmic bridges connecting

76  most plant cells [22]. This is supported by the association of plasmodesmata closing

77  (symplasmic isolation) and pressure build-up in specialized cells, such as guard cells or cotton

78  fibres [23–25]. However, pressure gradient was also observed in plant tissues with symplasmic

79  continuity [26], and predicted to be crucial for perception of water availability by roots [27]. In

80  addition, computational models of tissue mechanics suggest that neighbouring cells need to

81  have different pressure to recapitulate tissue arrangement and mechanical status in chemical-

82  treated Arabidopsis epidermis [28] and in Drosophila epithelia [29], although such spatial

83  variation is yet to be demonstrated, and its relation with cell-to-cell growth variability remains

84  elusive.

85  Here, we explore this issue in a model plant tissue, the epidermis of the *Arabidopsis thaliana*

86  shoot apical meristem (SAM), by combining computational modelling, dimensional analysis,

87  and experimental observations. Our physical model that couples tissue growth mechanics with

88  water movement accounts for our experimental observations of turgor pressure and growth rate

89  variability in different conditions. We show that cell pressure heterogeneity emerges from local

90  tissue topology to influence growth variability. Pressure level, however, is not a direct predictor

91  of growth rate, and dimensional analysis of the model reveals that growth behaviour depends

92  on the extent of the osmotic drive and on the balance between wall extensibility and hydraulic

93  conductivity. Together, we propose a link between cell topology and cell hydro-mechanical

94  status that may be involved in tissue homeostasis.

95  **Results**

96  **A mechanical-hydraulic model predicts pressure heterogeneity emerging from tissue**

97  **topology**

98  Earlier tissue models [28,29] retrieved intracellular pressure from static tissue geometry or

99  required differential osmotic pressure, whereas a recent model by Cheddadi et al. proposed that

4

100  both pressure and growth emerge from the coupling between cell wall mechanics and classical

101  plant hydraulics [30] in a tissue with hexagonal topology, i.e. with every cell having six

102  neighbours. We therefore tested, based on this model, the consequences of unequal neighbour

103  numbers on the mechanical status of the tissue, and notably on pressure (Fig. 1). We expanded

104  on the 2D vertex model to cell walls in a multicellular tissue with more realistic 2D polygonal

105  geometry. Generalizing the Lockhart-Ortega equation of visco-elasto-plastic 1D growth of

106  single cell (Fig. 1b) [20], each cell wall has a thickness $w$ and behaves as an elastic material of

107  modulus $E$ when wall tension induced by turgor pressure $P$ is low enough, more specifically

108  when the elastic strain $\varepsilon$ (reversible deformation) is lower than a threshold $\varepsilon^Y$. When tension in

109  the wall exceeds the corresponding threshold $E\varepsilon^Y$, the cell wall undergoes irreversible expansion,

110  akin to visco-plastic flow, with an extensibility (effective viscosity) $\Phi^w$ (Fig. 1c). Water flux

111  from extracellular space is proportional to $L^a\Delta\Psi$, where $\Delta\Psi = \Delta\Pi - P$ is the cross-membrane

112  water potential difference (external pressure is assumed to be zero; for parsimony we set $\Delta\Pi$

113  constant) and $L^a$ is the conductivity of the cell membrane. Intercellular water redistribution via

114  plant plasmodesmata [31], animal gap junctions, or cytoplasmic bridges [32,33] is driven by

115  intercellular differences in turgor pressure $P$, with a conductivity $L^s$. We did not prescribe turgor

116  pressure, instead letting it emerge from local mechanical and hydraulic interplays (see STAR

117  Methods for detailed model description).

118  To prescribe cell divisions, we utilized the recently introduced Willis-Refahi rule that derives

119  from experimental data in the SAM: cells divide according to their size and to the size increment

120  since the previous division [34]. The simulations recreate distributions of neighbour number

121  (topological distributions) that are similar to those observed in the SAM (Fig. 1e).

122  We set the model parameters based on classical measurements from Boyer [35] and Cosgrove

123  [36] (Table 1). We found turgor pressure to be heterogeneous, with a clear anticorrelation with

124  topology: cells with less neighbours have relatively higher pressure (Fig 1f, 3 simulations, cell

125  number $n = 1535$, Pearson correlation coefficient $R = -0.57$, $p < 10^{-100}$).

126

| Initial parameter | Value | Initial parameter | Value |
|---|---|---|---|
| Unit length | 10 μm | Apoplasmic | |
| Cell height $h$ | 10 μm | conductivity $L^a$ | $3.4 \times 10^{-10}$ m MPa$^{-1}$ s$^{-1}$ |
| Cell wall thickness $w$ | 1 μm | Symplasmic | |
| Elastic modulus $E$ | 33.8 MPa | conductivity $L^s$ | $3.4 \times 10^{-10}$ m MPa$^{-1}$ s$^{-1}$ |
| Wall extensibility $\Phi^w$ | $2.4 \times 10^{-5}$ MPa$^{-1}$ s$^{-1}$ | Osmotic pressure $\Delta\Pi$ | 0.7 MPa |
| Strain threshold $\varepsilon^Y$ | 0.1 | | |

| Perturbation | Modified parameter | Perturbation | Modified parameter |
|---|---|---|---|
| $\alpha^s = 0.1$ | $L^s = 3.8 \times 10^{-11}$ m MPa$^{-1}$ s$^{-1}$ | $\theta = 10 / 3$ | $\Delta\Pi = 1$ MPa |
| $\alpha^s = 0.9$ | $L^s = 3.1 \times 10^{-9}$ m MPa$^{-1}$ s$^{-1}$ | $\theta = 20 / 3$ | $\Delta\Pi = 2$ MPa |
| $\alpha^a = 0.1$ | $\Phi^w = 2.2 \times 10^{-4}$ MPa$^{-1}$ s$^{-1}$ | $\theta = 10$ | $\Delta\Pi = 3$ MPa |
| $\alpha^a = 0.9$ | $\Phi^w = 2.7 \times 10^{-6}$ MPa$^{-1}$ s$^{-1}$ | $\theta = 40 / 3$ | $\Delta\Pi = 4$ MPa |

**Table 2. Parameters used for the untreated model.** (Upper) The initial parameters correspond to $\alpha^s = 0.5$, $\alpha^a = 0.5$, $\theta = 7/3$ in Figure 1f, which are based on measurements by Boyer (1985) [35] for $\alpha^a$ and $\theta$, while $\alpha^s$ data is not available thus is conservatively ascribed an intermediate value of 0.5. (Lower) Non-dimensional parameter exploration around the reference values (initial parameters, except , $\theta = 20/3$) and the corresponding modified parameters. Note that $\alpha^a = 0.9$ corresponds to measurements by Cosgrove (1985) [36], compiled by Ortega (2019) [37].

In order to test the robustness of this result, we explored the parameter space of the vertex model. Analytical exploration in a two-cell system [30] had showed that systems dynamics is mostly controlled by three dimensionless parameters. The first, $\alpha^s$, compares intercellular water conductivity to total (intercellular and transmembrane) conductivity,

$$\alpha^s = \frac{A^s L^s}{A^s L^s + A^a L^a}$$

with $A^a$ the average surface of a cell, $A^s$ the average surface of a cell in contact with neighbouring cells, $L^a$ the conductivity (per unit surface) of the plasma membrane, and $L^s$ the conductivity (per unit surface) due to plasmodesmata. The second, $\alpha^a$, compares the limitation of growth by transmembrane conductivity to the combined limitation of growth by cell wall extensibility and transmembrane conductivity,

6

143
$$\alpha^a = \frac{L^a}{L^a + \Phi^w \dfrac{h^2}{4w}}$$

144 where $h$ and $w$ are cell height and cell wall thickness. Both $\alpha^s$ and $\alpha^a$ are bound between

145 0 and 1. The third parameter, $\theta$, assesses the osmotic drive by comparing the cross-membrane

146 osmotic pressure difference, $\Delta\Pi$, and a representative threshold pressure for growth to occur,

147 $P^Y$,

148
$$\theta = \frac{\Delta\Pi}{P^Y}$$

149 Contrary to the Lockhart-Ortega model that was formulated at cell scale, our model accounts

150 for specific cell wall geometry and mechanical properties. Accordingly, we express the

151 threshold in terms of a yield strain $\varepsilon^Y$ and the threshold pressure depends on cell geometry and

152 topology. We found empirically [30] that half the threshold pressure of a single hexagonal cell

153 provides a good order of magnitude for the threshold pressure in the multicellular model and

154 hence use

155
$$P^Y = \frac{w}{2R\cos(\pi/N)} E\varepsilon^Y$$

156 where $R$ is a representative cell size and the number of cell neighbours is $N = 6$ (Fig. S1).

157 The tissue globally grows if $\theta$ is greater than 1. Our first results, obtained with $\alpha^s = 1/2$,

158 $\alpha^a = 1/2$, and $\theta = 7/3$, corresponded to a balance between mechanical and hydraulic

159 limitations to growth (Fig. 1f). We explored the parameter space by considering 4 values of $\theta$

160 reaching up to 40/3 (Fig. 1i, S2). As will be clarified below (see last subsection), we considered

161 $\theta = 20/3$ as a reference value (Fig. 1g). We then decreased and increased either $\alpha^s$ or $\alpha^a$

162 down to 0.1 or up to 0.9, respectively (Fig. 1i, S2). Note that the values 0.5 and 0.9 of $\alpha^a$ span

163 available measurements of extensibility and conductivity [35,36] (Table 1). Next, we tested the

164 effect of cell divisions by arresting them (Fig. 1h). In all cases, we recovered the turgor–

165 neighbour-number anticorrelation (Fig. 1f-i, S2), demonstrating that topology-related pressure

166 heterogeneity is a robust behaviour of the model.

167 In simulations, like in SAM surface, cell neighbour number and size are coupled (Fig. 1f-i, S2).

168   Consistently, cell-specific turgor pressure anticorrelates with normalized cell area (Fig. 1f-I,

169   S2). To uncouple cell size and topology, we modified the initial state of our simulation to have

170   four-neighboured cells bigger than eight-neighboured cells, and found that higher turgor

171   pressure accumulated in four-neighboured cells, not in the smaller cells (Fig. 1j), showing that

172   turgor pressure heterogeneity emerges from tissue topology rather than cell size differences.

173   This can be explained by local topology, which determines cell wall angles and the subsequent

174   tension distribution at each tricellular junction (Fig. 1k, l): in our model, wall stress and strain

175   above the growth threshold are relaxed at a rate limited by wall extensibility and hydraulic

176   conductivity. Therefore, stress and strain are relatively homogenised in non-dividing

177   simulations (Fig. 1h), and the sum of wall tension at each tricellular junction (vertex) mostly

178   depends on the angles between walls. The vertex between three hexagonal cells with 120°

179   internal angles has a sum of tension at zero (Fig. 1k). Fewer-neighboured cells have sharper

180   internal angles, so the sum of tension at vertex is greater towards the cell interior, creating

181   additional inward compression and prompting higher pressure build-up at equilibrium (Fig. 1l).

182   In dividing simulations, new walls do not bear stress right after division because they form from

183   cell interior. These new walls are gradually strained due to mesh growth but do not yield

184   (expand) to release stress before reaching the threshold (Fig. 1f, g). Consequently, cell division

185   keeps the wall stress from homogenizing and dampens the turgor–neighbour-number

186   anticorrelation, compared to non-dividing simulations (Fig. 1g).

187   Altogether, our results imply that local hydrostatic pressure heterogeneity does not require

188   differential cellular osmotic pressure [28] in a growing tissue, and predict a topological origin

189   of pressure variability.

**Atomic force microscopy reveals heterogeneous turgor pressure in Arabidopsis shoot**
190   
191   **apical meristem**

192   To test predictions, we built upon recent advances in atomic force microscopy (AFM) that

193   enabled non-invasive turgor pressure retrieval utilizing indentation force-displacement and

194   surface topography in living plant cells (Fig. 2) [38–42]. We used a pressurized thin-shell model

195   to deduce the turgor pressure value from the AFM-measured force-displacement curves, which

196   are influenced by turgor pressure, cell wall mechanical properties, cell 3D geometry [38], and

197 may reflect mechanical properties at different sub- to supra-cellular scales according to

198 indentation depths (Fig. 2b-e). We applied AFM measurements to the Arabidopsis SAM

199 epidermis, a system featuring substantial growth heterogeneity [1]. We included untreated soil-

200 grown SAMs (Fig. 3) and a conceptually simpler model SAM co-treated with

201 naphthylphthalamic acid (NPA), a polar auxin transport inhibitor that induces pin-formed

202 SAMs, and oryzalin, a microtubule-depolymerizing drug that blocks cell division but permits

203 continuous, isotropic growth; hereafter referred to as "oryzalin-treated SAMs" (Fig. 4) [28].

204 Walls between cells are often curved in growing oryzalin-treated SAMs, suggesting that

205 neighbouring cells have different turgor pressure [28] in a growing tissue.

206 Figure 2 illustrates the AFM measurement pipeline, where we determined SAM surface

207 topography with AFM (Fig. 2f) and performed indentations near the cell centre to have near-

208 perpendicular indentation and minimize any bias due to surface slope (Fig 2g). Physical values

209 required to deduce pressure using the published formula [39,40], except cell wall thickness

210 separately measured by electron microscopy (EM), are simultaneously determined by AFM

211 scan and indentation. Specifically, both mean curvature $\kappa_M$ and Gaussian curvature $\kappa_G$ of outer

212 cell walls directly contribute to the capacity to sustain turgor pressure [38,39,43], and were

213 determined from AFM scan topography (Fig. 2f). As previously suggested in tomato SAM [44],

214 outer periclinal wall thickness is not very variable between cells or within cells in Arabidopsis

215 SAM, with untreated meristem $t_u$ = 179 ± 7 nm (mean ± standard error of mean, SEM) and

216 oryzalin $t_o$ = 742 ± 29 nm (Fig. S3). Based on previous work [45], we used the indentation

217 depth range 0 to 150 nm to determine apparent Young's modulus of cell wall, $E$ (Fig. 2b, e). We

218 determined indentation stiffness, $k$, using the depth range 0.3 to 0.5 μm for untreated and 1.1 to

219 1.5 μm for oryzalin-treated meristems (Fig. 2c, e); these ranges were chosen so that depth is

220 greater than wall thickness (to minimize cell wall contributions to $k$) and the deformed region

221 remains smaller than cell size (to minimize the contributions of neighbouring cells to $k$, Fig. 2d,

222 e), so as to be in the validity range of the pressurized shell model [40]. Note that these values

223 of depth for untreated SAMs differ from the larger values (1 to 2 μm) used in preliminary

224 experiments [41], which were interpreted using supracellular curvature (unlike here) and were

225 chosen to reveal supracellular pressure (averaged over many cells and possibly over cell layers)

9

226    for comparison with the large-scale pressure obtained using indentation with a large flat tip

227    (100 μm diameter). To verify the validity of the depth ranges used here, we tested influence of

228    tissue context on indentation readout [46] by numerical simulations of indentations on realistic

229    3D meshes accounting for pressurized epidermal cells (Fig. 2m-o''); in conditions

230    corresponding to experiments, the deformation of neighbouring cells was negligible,

231    demonstrating that the depth range enables cell-level measurements.

232    Cell-specific AFM indentations on seven untreated and nine oryzalin-treated SAMs revealed

233    that surface wall curvature, Young's moduli, cell apparent stiffness and the deduced turgor

234    pressure are all markedly heterogeneous across SAM epidermis (Fig. 3, 4). We computed

235    intracellular variability of quantities measured at subcellular scale (which excludes curvature,

236    measured at cell scale), and found that apparent Young's modulus $E$ and stiffness $k$ show

237    significantly higher variability than pressure $P$ (as quantified by intracellular coefficients of

238    variation, Fig. 3i, 4i), which agrees with previous work [40], and supports deduced $P$ being a

239    cellular property. Additionally, we found that $E$ shows relatively comparable subcellular and

240    intercellular variability, as previously observed [45,47], whereas $P$ show significantly bigger

241    heterogeneity between than within cells (Fig. 3j, 4j). Deduced pressure, $P$, is relatively

242    insensitive to variability in thickness as described in [40], and change in thickness by $1\times$

243    standard deviation (SD) only alters the coefficient of variance (CV) of $P$ by 3% and 9% for

244    untreated and oryzalin-treated samples respectfully, both significantly smaller than the

245    intercellular $P$ variability (untreated 21% and oryzalin 15%). All these indicate that $P$ deduction

246    is cell-specific, and that variability in cell wall mechanics does not account for deduced pressure

247    heterogeneity.

248    **Osmotic treatments reveal large values of osmotic pressure in the shoot apical meristem**

249    Based on AFM, we find that deduced turgor pressure is heterogeneous, with averages values

250    per meristem of $2.61 \pm 0.03$ MPa and $1.21 \pm 0.34$ MPa (mean $\pm$ SEM) in untreated and oryzalin-

251    treated meristems, respectively (Fig. S3). These values appear high with respect to the classical

252    0.3 to 1 MPa range found in most other plant tissues, though values of up to 5 MPa were

253    measured in guard cells of other species using the pressure probe [48].

254    As neither the classic pressure probe nor the pico gauge [49] can be applied to cells as small as

255    in the shoot apical meristem, we assessed quantitatively the values of turgor pressure $P$, by

256    using an incipient plasmolysis assay to determine the osmotic pressure of SAM, and found that

257    untreated meristems had a rather invariable osmolarity of about 0.5 Osm, slightly higher than

258    values reported in tomato SAM [50], while oryzalin samples showed a wider variability of 0.6

259    to 1.0 Osm (Fig. S4). The corresponding values of osmotic pressure, 1.2 MPa for untreated and

260    2.0 MPa for oryzalin treated, are comparable to the values of AFM-deduced turgor (2.6 MPa

261    and 1.2 MPa, respectively) (Fig. S3, S4). The quantitative agreement is less good in the case of

262    untreated meristems, possibly due to tissue tension in the epidermis which could artificially

263    increase the deduced pressure due to contributions from inner layers. We note however that

264    tissue tension would smooth out intercellular differences and would thus not contribute to the

265    cell-to-cell heterogeneity of pressure. An alternative explanation would be that solute

266    penetration differs between untreated and treated SAMs. Altogether, the values of turgor found

267    with AFM are in semi-quantitative agreement with the values of osmotic pressure deduced from

268    incipient plasmolysis.

269    **Cell pressure in shoot apical meristem anticorrelates with local topology and size**

270    Next, we tested model predictions and found that, indeed, AFM-determined cellular pressure

271    anticorrelates with the number of epidermal cell-neighbours $N$, or local topology (7 SAMs, $n =$

272    503 cells, $R = -0.16$, $p = 10^{-4}$, Fig. S5). With the linear relationship between cell area and

273    neighbour number (Fig. 3d) due to fundamental geometrical constraints in compact tissues [51],

274    we also identified strong anticorrelation between pressure and cell size $A$ ($R = -0.19$, $p = 10^{-5}$).

275    We focused on cell-to-cell turgor variations and we removed variations between SAMs by

276    normalizing cellular pressure to the average pressure per SAM; given that untreated SAMs have

277    unvaried average turgor values (Fig. S3), the anticorrelation is conserved for pressure-versus-

278    topology ($R = -0.16$, $p = 10^{-4}$) and versus-size ($R = -0.23$, $p = 10^{-7}$) (Fig. 3h-h'').

279    Encased in rigid cell walls, plant cells seldom exchange neighbours, and the main source of

280    topological change is via division, where dividing cells tend to lose neighbours and cells

281    adjacent to the division plain tend to gain neighbours [52]. We therefore considered oryzalin-

282    treated SAM, in which cell divisions are arrested while growth is continuous, and recovered

11

283   similar anticorrelation for pressure against neighbour number (9 SAMs, $n$ = 202 cells, $R$ = -

284   0.19, $p$ = 0.008) and against cell area ($R$ = -0.48, $p$ = $10^{-12}$) (Fig. S5). Normalization further

285   enhanced the pressure-versus-topology anticorrelation ($R$ = -0.31, $p < 10^{-5}$) while preserving

286   the pressure-size trend ($R$ = -0.33, $p < 10^{-5}$) (Fig. 4h-h''), indicating that the pressure-topology

287   and pressure-size relationships are robust system-level trends, regardless of the absolute values.

288   We then examined whether such trends may be caused by trends in cell wall thickness, $t$, or

289   modulus, $E$, or by trends in stiffness, $k$. There is no correlation between $t$ and cell size ($R$ = -

290   0.10, $p$ = 0.65, Fig. S3). So $t$ only introduces small unbiased noise, and it cannot account for

291   the $P$ heterogeneity. We found that $E$ and $k$ showed no significant correlation to cell neighbour

292   number $N$ in untreated SAMs (Fig. 3e-f'), indicating that they introduce no systemic bias to $P$

293   heterogeneity. In oryzalin-treated SAMs, however, both $E$ and $k$ showed weak positive

294   correlation to $N$ (Fig. 4e-f'), which is opposite to the $P$ vs $N$ anticorrelation (Fig. 4h'). This is

295   interesting, because the higher $P$ in $N$ = 4 cells cannot be explained by lower $E$ and $k$ ("softer"

296   cell). This indicates that, although feedback from shape on $E$ may occur in oryzalin-treated

297   meristems, $P$ heterogeneity is not a direct consequence of feedbacks from wall tension or cell

298   geometry/topology on wall stiffness.

299   Moreover, we found that turgor pressure heterogeneity may be removed when sample is

300   osmotically challenged: the same SAM shows heterogeneous pressure when turgid and

301   homogeneous pressure when at intermediate turgidity (Fig. S4). This shows that the AFM

302   approach is not technically biased by tissue topology and/or cell size.

303   Finally, we used cell side wall convexity as a proxy for differences in turgor, because cells with

304   higher pressure would be expected to bulge out into cells with lower pressure (Fig. 4q-q'') [53].

305   We constructed a weighed convexity index (wCI) to quantify convexity (Fig. 3o-q, 4o, p), and

306   found that convexity significantly anticorrelates with number of neighbours, in agreement with

307   qualitative observations in oryzalin-treated meristems [28], and in agreement with the pressure

308   trends.

309   Altogether, our data indicate that non-random turgor pressure heterogeneity establishes in

310   tissues with static topology (no neighbour number change) or dynamic topology (neighbour

311    numbers change due to division). Although tissue topology is sufficient to explain pressure

312    heterogeneity, we do not exclude a role of other biological parameters and/or sources of noise

313    in pressure variations, as suggested by weaker correlations in experiments (Fig. 3h', 4h') than

314    in simulations (Fig. 1g, h).

315    **Realistic mechanical models of tissue indentation are inconsistent with homogeneous**

316    **pressure**

317    Whereas the aforementioned pressure deduction is based on a model utilizing local cell shape

318    [39], Mosca et al. [46] proposed that cell packing also contribute to the indentation stiffness.

319    We therefore implemented realistic indentation using a thin-shell indentation finite element

320    method (FEM) model following Mosca et al. [46]. We constructed two realistic templates

321    (untreated- and treated-like) from confocal images; the surface was meshed and the outermost

322    cell layer was constructed to represent the epidermis, with uniform values of cell wall thickness

323    taken from our EM-based measurements and same cell dimensions as in confocal images; all

324    cells were inflated by turgor pressure (Fig. 2m). We used the null hypothesis that all cells were

325    inflated by uniform turgor pressure (2 MPa, rounded from experimental values), and performed

326    indentations on the exact corresponding cells indented experimentally from these two templates,

327    excluding cells at periphery of the template to avoid boundary effects. We chose indentation

328    near the cell centre to have near-perpendicular indentation, like in experiments. We recovered

329    values of apparent stiffness $k$ that have the same magnitude as experimental values: untreated-

330    like $k_{FEM} = 14.9 \pm 0.1$ N/m (mean $\pm$ SEM, compared to $k_{AFM} = 12.9 \pm 0.2$ N/m), treated-like

331    $k_{FEM} = 38.2 \pm 1.0$ N/m (compared to $k_{AFM} = 14.5 \pm 0.6$ N/m). However, we found that the $k$

332    variability differs from experiments, notably in untreated SAMs (Fig. 3k, 4k). Closer inspection

333    revealed that cell surface mean curvature $\kappa_M$, which is directly linked to $P$, also showed strong

334    discrepancy between simulation and experiment (Fig. 3l, 4l). Accordingly, the null hypothesis

335    of uniform turgor is not consistent with experimental data. We corrected such discrepancy based

336    on the theory of thin shells (apparent stiffness mainly depends on these two parameters

337    following $k \sim \pi P \kappa_M^{-1}$, see [39]) by rescaling $\kappa_M$ and $P$ according to their experimental

338    variability, and recovered the heterogeneous distribution of $k$ determined by AFM (Fig. 3m,

339    4m). Conversely, correction of $k$ and $\kappa_M$ also recovered the experimentally deduced $P$

13

340     distribution. This indicates that the discrepancy between FEM and AFM indentations can be

341     fully explained by the heterogeneity in pressure (and subsequently curvature), and the

342     contribution of cell packing to the measured variability is negligible with our depths of

343     indentation.

344     **Two types of correlations between cell growth and local topology or size**

345     Next, we monitored areal growth rate of SAM epidermal cells by time-lapse confocal

346     microscopy. As observed previously, untreated SAMs exhibited slower growth in the centre,

347     where stem cells reside, than the surrounding cell [54] (Fig. S5). In addition, cellular growth

348     rate anticorrelates with neighbour number (11 SAMs, $n$ = 1491 cells, $R$ = -0.15, $p$ = $10^{-8}$; Fig.

349     5e) and cell size (Fig. 5f; $R$ = -0.33, $p$ = $10^{-38}$), supporting previous reports that smaller cells in

350     SAM grow faster [34,55], and suggesting that higher turgor pressure in fewer-neighboured cells

351     associates with faster growth. In oryzalin-treated SAMs, however, the fewer-neighboured and

352     small cells grew slower (14 SAMs, $n$ = 1160 cells; Fig. 5k, neighbour number $R$ = 0.20, $p$ = $10^{-11}$;

353     Fig. 5l, cell size $R$ = 0.16, $p$ = $10^{-8}$). This suggests that higher turgor pressure associates with

354     either faster or slower growth depending on conditions. Although seemingly a small shift, this

355     negative-to-positive slope change of local growth heterogeneity captures a strong qualitative

356     inversion of growth behaviour (Fig. 5d, j). Accordingly, smaller cells expand more than larger

357     cells in untreated SAMs, which may contribute to cell size homeostasis, a phenomenon that

358     would be absent in oryzalin-treated SAMs.

359     **Heterogeneity in growth rate is patterned according to the balance between wall**
360     **extensibility, tissue conductivity and osmotic drive**

361     We further explored the growth trend in our vertex model. Based on the parameter exploration

362     on dividing mesh aimed to reproduce untreated SAM behaviour, we found both positive and

363     negative correlations between growth rate and cell neighbour number (Fig. S2). This indicates

364     that growth trend is sensitive to parameters that alter the balance between water flux and wall

365     expansion (governed by the non-dimensional parameter $\alpha^a$) and to the ratio between osmotic

366     pressure and yield pressure ($\theta = \Delta\Pi/P^Y$). This can be rationalized by examining the relative

367     growth rate $G$ of a cell according to the Lockhart model (see [30]).

$$G = \alpha^a \Phi^w \frac{h}{2w}(\Delta\Pi - P^Y)$$

Both the prefactor $\alpha^a \Phi^w h/2w$ and the yield pressure $P^Y$ decrease with cell size $R$ and neighbour number N, while $\Delta\Pi$ is constant. Consequently two regimes are expected: when the osmotic drive $\theta$ is smaller than a threshold $\theta^T$, $G$ is dominated by the variations of $P^Y$, therefore $G$ increases with cell size and with neighbour number, which corresponds to the trend in oryzalin-treated meristems; when $\theta > \theta^T$, the variations of $P^Y$ are negligible, so $G$ follows the prefactor and decreases with cell size, which corresponds to the trend in untreated meristems. These two regimes occur whatever the value of $\alpha^a$, and the threshold value $\theta^T$ increases with increasing $\alpha^a$. In a tissue context, many global parameter shifts can invert growth trend through changes in these dimensionless parameters (Fig. 6k, l).

Overall, the model retrieves untreated SAM trends if transmembrane conductivity partially limits growth ($\alpha^a$ not too large), symplasmic conductivity is not on par with transmembrane conductivity ($\alpha^s$ not too large) or if the osmotic drive is sufficient (the ratio of osmotic to yield pressure is large enough). Conservatively, we chose equal contribution by flux and wall in our model ($\alpha^a = 0.5$), and increased osmotic pressure to 2 MPa, a value comparable to the experimental measurements: Figures 6a-c show that the fewer-neighboured and smaller cells grow faster (3 simulations, $n = 1496$; $G$ vs $N$, $R = -0.10$, $p = 10^{-4}$; $G$ vs $A$, $R = -0.76$, $p < 10^{-100}$).

We then attempted to reproduce oryzalin-treated behaviour, guided by the experimental observations that, besides stopping cell division, oryzalin treatment also yields higher osmotic pressure (1.6-fold) and drastically thicker cell walls (4-fold) (Fig. S3, S4). We found that both stalling division and increasing osmotic pressure failed to invert the growth trend in the model, as expected, while doubling and quadrupling wall thickness inverted the correlation of growth rate to neighbour number and cell size (Fig. 6d-j; S6), like in oryzalin-treated SAM. Combining higher osmotic pressure and thicker wall revealed that quadrupling wall thickness can robustly trigger growth trend inversion (Fig. 6j, S6).

Effectively, changing osmotic pressure and wall thickness alter the wall–flux limitation balance of the system (Fig. 6j-l). Higher osmotic pressure induces faster water influx (reduced limitation

15

395   by hydraulics). The extra volume strains the walls to accumulate stress farther beyond the

396   threshold, which is relaxed by wall yielding (growth) with extensibility as the rate limit.

397   Meanwhile, wall thickening reduces wall stress and strain towards the threshold for expansion,

398   effectively reducing the mechanical drive of growth and increasing the weight of water

399   permeability in limiting growth. We do not exclude other possible parameter changes triggered

400   by oryzalin treatment, like water conductivity and wall synthesis rate, that also contribute to the

401   wall–flux limitation balance. Nevertheless, implementing the observed cell wall thickening in

402   the model is sufficient to explain the observed growth rate inversion from untreated to oryzalin-

403   treated scenario.

404   **DISCUSSION**

405   In this study, we modelled the growth of a plant tissue by coupling tissue mechanics and tissue

406   hydraulics. This generalizes previous models focusing only on mechanics [56–58]. In this

407   model, both cell growth and turgor pressure emerge from mechanics and hydraulics. Each of

408   these parameters can be controlled by genetic and biochemical inputs, and small uniform

409   changes in these biological inputs can enable drastic shifts of system behaviour and the final

410   cell size distribution (Fig. 6m). We predicted that a broad distribution of neighbour number

411   leads to heterogeneity in cell growth and in turgor pressure, even when hydraulics has a minor

412   contribution to the control of growth. We verified this prediction in the context of the shoot

413   apical meristem (SAM) of *Arabidopsis thaliana*. It remains to be seen whether our results apply

414   to other plant tissues, to animals or whether this is specific to the SAM.

415   In order to test our predictions and deduce pressure in the SAM, we combined a recently

416   developed indentation-based approach [40] with FEM-based realistic mechanical models of

417   indentation [46]. We found values of turgor in the range 1-3 MPa range, higher than the range

418   0.2-1 MPa generally measured in plant tissues [18], though values of up to 5 MPa were

419   measured in guard cells [48]. For instance, the Arabidopsis root epidermis has a turgor of about

420   0.4 MPa, as measured with the pressure probe [59]; the Arabidopsis leaf epidermis has a turgor

421   of about 1-2 MPa, as deduced form indentation and mechanical modelling [60]. Accordingly,

422   we speculate that the SAM function might require relatively high turgor. Another specificity of

16

423   the SAM could be a relatively low transmembrane conductivity, as most aquaporin (channel

424   protein allowing rapid transmembrane water flux [61]) isoforms had significantly lower

425   expression in inflorescence than in other fast growing tissues like stem and root [62] (with a

426   reduction up to ~80%). Nevertheless, a wide range of water conductivity can produce pressure

427   heterogeneity, including very high conductivity (i.e. $\alpha^a = 0.9$ [36]), and the agreement between

428   model predictions and experimental measurements suggest that tissue hydraulics has a

429   (possibly small) contribution to limiting growth in the SAM. Similarly, altered expression of

430   the aquaporin PIP2;1 delays the emergence of lateral roots [63], also hinting to a developmental

431   role for hydraulic conductivity. Altogether, we propose that tissue mechanics and hydraulics act

432   in parallel with the established genetic regulations in SAM cell growth.

433   We found that both cell growth and turgor pressure are heterogeneous in the SAM. It has already

434   been reported that smaller cells [55] or the smaller of two sister cells [34] grow faster in the

435   SAM of untreated and NPA-treated plants, respectively. We found the same trend in untreated

436   SAM, with an inversion in oryzalin-treated SAM. Such inversion is not irrelevant to normal

437   development: for example, a growth variability switch is observed during sepal development,

438   where clones of smaller and often fewer-neighboured cells grow faster in young sepals then

439   slower in older sepals, effectively shifting from homogenizing to amplifying cell size variability

440   [64]. In untreated SAM, small cells grow faster than big cells, possibly contributing to tissue

441   homeostasis. Finally, irrespective of the conditions, we find that turgor pressure is smaller in

442   big cells in experiments, which might contribute to reducing mechanical stress in the cell wall

443   in these cells [65]; this would act in parallel with the mechanism proposed in the context of leaf

444   epidermal cells, based on cells adopting puzzle shapes that limit cell wall stress [65].

445   Our results point towards a link from cell topology (number of neighbours) to cell mechanical

446   status. This might also be relevant to animal epithelia [29], though this appears unexplored

447   experimentally. Feedbacks from cell mechanics to cell topology are more established: cell

448   division and thus number of neighbours can be oriented by mechanical stress in animals and in

449   plants [66–69]. Since tissue topology is highly conserved in many biological systems [70], we

450   propose that pressure heterogeneity may emerge in compact tissues with polygonal cells [63]

451   and non-instantaneous water movement, due to the adjustment to reconcile local mechanical

17

452 and hydraulic conditions.

453 Finally, we note that heterogeneous patterns may not always be stochastic [71]. The emergent

454 heterogeneity of local growth and hydrostatic pressure is coupled with the characteristic yet

455 dynamic tissue topology [51,52] (Fig. 6m), all based on stringent rules and likely underlies

456 morphogenesis in compact tissues. With the discovery of many cell-size-dependent transcripts

457 [3,72], our model proposes another source for non-random variability in a tissue.

458

459

460 **STAR Methods**

461 **Plant materials, treatments and growth conditions**

462 *Arabidopsis thaliana GFP-LTi6b* (ecotype WS-4) reporter line and ecotype Col-0 was used[73].

463 Untreated inflorescence meristems were obtained from soil-grown plants, first in short-day (8

464 h light 20°C / 16 h dark 19°C cycle) for 3 to 4 weeks then transferred to long-day (16 h light

465 20°C / 8 h dark 19°C cycle) for 1 to 2 weeks to synchronize bolting. Oryzalin-treated

466 inflorescence meristems were obtained from plants grown on custom-made Arabidopsis

467 medium [74] (Duchefa) supplemented with 1% agar-agar (Merck) and 10 μM N-1-

468 naphthylphthalamic acid (NPA, Sigma-Aldrich/Merck) for 3 weeks. Pin-formed inflorescence

469 meristems from NPA medium were immersed in 10 μg/mL oryzalin (Sigma-Aldrich/Merck)

470 twice (3 h duration, 24 h interval) [28]. For mechanical measurements and time-lapse confocal

471 imaging, meristems were mounted on Arabidopsis apex culture medium (ACM) [74] with 2%

472 agarose and 0.1% plant preservation mixture (PPM, Plant Cell Technology) to prevent

473 contamination, and cultivated in long-day condition.

474 **Atomic force microscopy**

475 Untreated meristems (dissected, with most late stage-2 floral primordia removed to prevent

476 blocking of the cantilever) and oryzalin-treated meristems were mounted on ACM (2% agarose,

477 0.1% PPM) the night before. Drops of 2% low melting agarose (Duchefa) were applied around

478    the lower parts of meristems for mechanical stabilization. For oryzalin-treated meristems, 72 h

479    post-treatment meristems were measured.

480    AFM indentations were performed as in Beauzamy et al., 2015 [40]. Specifically, a BioScope

481    Catalyst model AFM (Bruker) operated with the NanoScope software (version 9.1, Bruker),

482    under a MacroFluo optical epifluorescence macroscope (Leica), was used. All measurements

483    were done with customized 0.8 μm diameter spherical probes mounted on silicon cantilevers

484    of 42 N/m spring constant (SD-Sphere-NCH-S-10, Nanosensors). Cantilever deflection

485    sensitivity was calibrated against a clean sapphire wafer submerged in water before each session.

486    Meristems were submerged in water during AFM measurements. PeakForce QNM mode was

487    used to record sample surface topography and cell contours (aided by the stiffness difference

488    between periclinal and anticlinal cell walls on DMT modulus maps) in overlapping square tiles

489    of $30\times30$ to $50\times50$ μm$^2$ ($128\times128$ pixels). Force curves were obtained by the point-and-shoot

490    mode of the NanoScope software, with at least 3 locations chosen near the barycentre of each

491    cell, and 3 consecutive indentations per location, making at least 9 force curves per cell.

492    Approximately 10 μN maximum force was applied during each indentation, corresponding to

493    approximately 1 μm indentation depth.

494    For hyperosmotic treatments, oryzalin-treated meristems were mounted in Petri-dishes on

495    Patafix (UHU), then the gap between Patafix and sample base was quickly sealed with bio-

496    compatible glue Reprorubber-Thin Pour (Flexbar) for stabilization. After the glue solidified

497    (less than 2 minutes), samples were submerged in liquid ACM containing 0.1% PPM. Samples

498    were first measured in liquid ACM (plus 0.1% PPM), then submersion medium was changed

499    to ACM plus desired concentration of NaCl (plus 0.1% PPM) by first rinsing with 3~5 mL

500    target solution, then soaked in target solution for 5 minutes before AFM measurements. Each

501    new measurement per solution change took around 30 minutes.

502    **Force curve analysis**

503    Turgor pressure was determined as previously reported [40]. Specifically, cell wall elastic

504    modulus (Hertzian model, 1~10% maximal indentation force) and cell apparent stiffness (linear,

505    75~99% maximal indentation force) were retrieved from each force curve by the NanoScope

506    Analysis software (version 1.5, Bruker). Quality of force curves were checked empirically and

507    by the fit coefficient of determination $r^2 > 0.99$. Cells with only low quality force curves were

508    not analysed. Cell surface curvatures (mean and Gaussian) were estimated from AFM

509    topographic images, with the curvature radii fitted to the long and short axes of each cell. Turgor

510    pressure was further deduced from each force curve (100 iterations) with the electron-

511    microscopy-determined cell wall thickness 190 nm for untreated and 740 nm for oryzalin-

512    treated SAMs, and cell-specific turgor pressure is retrieved by averaging all turgor deductions

513    per cell.

514    For cell registration, confocal stacks of each meristem were obtained prior to AFM

515    measurements by an LSM 700 confocal (Carl Zeiss). Surface projection of *GFP-LTi6b* signal

516    was generated by the software MerryProj [75], then rescaled and rotated (affine transformation)

517    to overlay the AFM image tiles. The resulting surface projection image was used to generate

518    cell contour image of the whole meristemic surface using morphological segmentation plugin

519    [76] for the software ImageJ (https://fiji.sc/), while the relative positions of each AFM

520    indentation location is then registered onto the cell contour image, along with cellular

521    geometrical and topological analyses, using the NanoIndentation plugin (version alpha) for

522    ImageJ [77].

523    Since each meristem had different turgor pressure range, cellular turgor pressure was

524    normalized to the average of each meristem for comparing cell-to-cell turgor pressure

525    heterogeneity without meristem-specific effects.

526    **Electron microscopy**

527    For serial block-face imaging SEM (SBF-SEM), plants were grown in vitro on medium

528    containing the auxin transport inhibitor NPA (Naphtalene Phtalamic Acid) to generate stems

529    with naked meristems and were locally treated for 48h with the microtubule depolymerizing

530    drug oryzalin (Sigma) in lanolin at a concentration of 2 μg/μl [78]. These plantlets were

531    subsequently taken off the inhibitor and left to regenerate for 48h on normal Arabidopsis

532    medium. Meristems with young organ primordia were fixed in 0.5% glutaraldehyde (in

533    demineralized water), from 25% Sigma stock in Microscopy Facility lab. The plantlets were

20

534  left at room temp for 2h in an eppendorf and rinsed 1x in water before post fixation and de-

535  hydrating and embedding in Spurr's epoxy as described in [79]. The samples were then

536  sectioned and viewed in a Zeiss Merlin SEM [79].

537  For standard transmission electron microscopy fixed meristems of soil grown plants were

538  embedded in Spurr's resin and sectioned before viewing in a Jeol 2100F (at the Centre

539  Technologique des Microstructures, UCBL, Lyon).

540  **Time-lapse confocal microscopy**

541  Untreated (dissected) and oryzalin-treated meristems were mounted and grown on ACM with

542  0.8% agarose and 0.1% PPM for live imaging. Confocal stacks were taken on an LSM 700

543  confocal microscope (Carl Zeiss) operated with the ZEN 2010 software (version 6.0, Carl

544  Zeiss), using a W N-Achroplan 40x/0.75 M27 water immersion objective, and on a TCS SP8

545  confocal microscope (Leica) operated with the Leica Application Suite X software (version 3.5,

546  Leica), using a Fluotar VISIR 25x/0.95 water immersion lens. GFP was excited at 488 nm and

547  emission detected between 415 – 735 nm. Stacks have resolution of $1028\times1028$ pixels, with

548  resolution ranging between 3.2 to 4.4 pixels/μm; Z steps were between 0.5 and 0.85μm.

549  For hyperosmotic treatments, meristems were mounted in Petri-dishes on Patafix (UHU), then

550  submerged in liquid ACM containing 0.1% PPM. Samples were first imaged in liquid ACM

551  (plus 0.1% PPM), then submersion medium was changed to ACM plus desired concentration

552  of NaCl (plus 0.1% PPM) by first rinsing with 3~5 mL target solution, then soaked in target

553  solution for 5 minutes before imaging. Because of the reduced signal in hyperosmotic solutions,

554  possibly due to the altered refractive index, stronger gain was used to reach comparable signal

555  intensity.

556  **Image processing and geometric analysis**

557  3D shell mesh and surface projection of untreated meristems were generated from confocal

558  stacks using the level set method (LSM) addon [80] for the software MorphoGraphX (MGX

559  version 1.0) [81]. For oryzalin-treated meristems, 2D surface projections were generated by

560  MerryProj [75] and imported into MGX for further processing. Projected images were

21

561 segmented using watershed method after manual seeding, and cell lineage between time points

562 was manually assigned in the meristem proper. To limit Z distortion and biases due to change

563 in inclination of the surface, which may affect analysis accuracy, only cells within 20° of

564 inclination angle from the highest position of the SAM were included. A custom-made Python

565 script was used to trace cell lineage between multiple time points and determine cell topology

566 based on the anticlinal wall number exported from MGX. Areal relative exponential growth

567 rate per hour was calculated as:

568
$$G = \frac{\ln(A_t/A_0)}{\Delta t}$$

569 where $\Delta t$ is time interval in hours, $A_0$ is original cellular area at time $t_0$, and $A_t$ is final area at

570 time $t_0 + \Delta t$. Cells undergone topological changes (i.e. divided cells and cells adjacent to new

571 division planes) during the acquisition were not included in the growth analyses. To analyse

572 variation, cell-specific growth rate was further co-aligning by the median per SAM then

573 stretching the distribution to the average first and third quartile positions to each data point.

574 To enhance the confocal images in hyperosmotic solution, anisotropic diffusion filter [82] was

575 re-implemented and applied to the raw images with the following parameters (specifications

576 see http://cbp-domu-forge.ens-lyon.fr/redmine/projects/anifilters/wiki): $K = 0.3$, $\sigma = 5$, $\gamma = 0.9$,

577 $D = 10$, 50 iterations.

578 For figure panels, brightness and contract of confocal images were linearly enhanced for better

579 visual. To synchronize panel shape and size, black background with no relevant information

580 was cropped from or added to the edge of the panels.

581 **Finite element method (FEM) indentation simulation**

582 Inflation and indentation simulations were performed with the same procedure adopted from

583 Mosca et al., 2017 [46]. For each meristem, a surface projection of the L1 anticlinal walls

584 obtained from confocal microscopy was segmented and extruded to the average anticlinal wall

585 height as observed in the template (5 μm for untreated and 10μm for oryzalin-treated) with the

586 CellMaker plugin for MorphoGraphX [81]. This generates a multicellular template made of

587 triangular membrane elements. The extruded meshes keep the average overall organ curvature.

588    In order to give the extruded cells a more realistic rest curvature (in the unpressurized state),

589    both meshes were pre-inflated with a small pressure (0.05 MPa for untreated and 0.15 MPa

590    oryzalin-treated SAM) and saved as the rest configuration. Both meshes were refined around

591    the indentation points to increase the accuracy of the indentation simulations. The untreated

592    mesh used in the indentation simulation and curvature analysis has an average edge size of 0.1

593    μm near the indentation points and increases to 0.5 μm far away from those points. The

594    oryzalin-treated mesh has instead an average edge size of 0.2 μm and 1 μm near and far from

595    the indentation the indentation areas, respectively.

596    The cell wall was modelled as a Saint-Venant Kirchhoff material represented by membrane

597    elements with zero transversal stress and mathematically prescribed thickness [46]. The two

598    templates were assigned the following material properties:

599      - isotropic material, 200 MPa Young's modulus, 0.3 Poisson ratio;

600      - cell wall thickness of 0.19 μm and 0.74 μm for the untreated and oryzalin-treated meristem,

601        following experimental data.

602    The templates were inflated from the rest configuration with a turgor pressure of 2 MPa inside

603    each cell for both meshes, until the forces equilibrium was reached (sum of the forces squared).

604    With the chosen parameters, the total cell height after inflation is similar to the experimental

605    observation from the confocal stacks for the referring templates (6.8 μm for untreated and 14.5

606    μm for oryzalin-treated). Afterwards the bottom of the template (bottom anticlinal cell walls)

607    was blocked in all space degrees of freedom to simulate the presence of the supporting inner

608    tissue during the indentation process.

609    The indentation is modelled as in [46] and is performed in the global z-direction as given by

610    the confocal images. The indentation process is performed on each cell independently, where

611    the specific indentation point is chosen to be close to the uppermost anticlinal wall location.

612    This reproduces the AFM indentation modality. As in analysis of AFM experiments, the

613    stiffness of the untreated cell was computed as the slope of the indentation curve at 0.5 μm

614    indentation depth, with the reaction forces on the indenter between 0.3 and 0.7 μm depth used

23

615  for slope computation. For the oryzalin-treated, given the thicker walls, the indentations were

616  deeper and the stiffness was computed around 1 μm indentation depth (reaction forces between

617  0.8 and 1.2 μm).

618  For both meshes, a refinement analysis was performed to verify the accuracy of the simulation

619  results. The results are reported in Supplementary Table 1. We considered the variation of the

620  coarse oryzalin mesh so small to justify using it for the AFM and curvature comparison analysis,

621  while we preferred using the refined mesh for the untreated to reduce the error due to mesh

622  resolution.

| Mesh | coarse size | refined size | Relative MD | sd of relative MD |
|---|---|---|---|---|
| Untreated | 0.2 μm | 0.1 μm | 3% | 2.4% |
| Oryzalin-treated | 0.4 μm | 0.2 μm | 2% | 1.3% |

623  **Supplementary Table 1. FEM refinement analysis.** Coarse mesh edge size near

624  indentation; refined mesh average edge size near indentation; relative MD, relative mean

625  absolute difference; sd, standard deviation.

## Statistical analysis

627  Data were processed using Excel 2000 (Microsoft). All Tukey box plots depict the first, second

628  (median) and third quartiles of data distribution, with whiskers marking the lowest/highest data

629  within 1.5 interquartile ranges (IQR) of the lower/upper quartiles. Tukey's outliers are depicted

630  as small circles outside the whiskers. Values like turgor pressure, cell area and growth rate were

631  normalized to the average per meristem. After normalization, every cell was considered as one

632  biological sample, and all linear regressions and Pearson correlations were performed on whole

633  datasets. For simulations, cells on the edge of the mesh were not analysed due to border effect.

634  Extremely rare polygon classes (i.e. triangle and nonagon) were not shown on the box plots in

635  the main figures but were included in linear regression and Pearson correlation tests and were

636  plotted in Figure S5. Kolmogorov–Smirnov test was used to distinguish cell neighbour number

637  distribution (significance level $\alpha = 0.05$).

## Mechanical-hydraulic modelling

639    *Summary.* We build a vertex-based model of plant tissues at cellular level that couples osmosis-

640    driven hydraulic fluxes between cells and from apoplast with a fixed water potential, and cell

641    wall mechanics which resists and grows under tension. Turgor and growth rate heterogeneities

642    emerge from this coupling and from the heterogeneities in cells sizes and topology (number of

643    neighbours).

644    We consider a collection of $N$ polygonal cells $i = 1, \ldots, N$ that form a mesh; this mesh evolves

645    with the appearance of new cells because of cell division. The walls between cells are

646    discretized into one or several segments. Given the topology, the mesh is fully characterized by

647    the position of the vertices. The walls are given a height $h$ and a thickness $w$.

648    *Cell wall rheology.* The cell walls are modelled as a visco-elasto-plastic material, which would

649    be equivalent to the Ortega model [20] in the case of an elongating cell. Let $\sigma_k$ be the stress of

650    a wall segment $k$; the constitutive law writes $\sigma_k = E_k \varepsilon_k^e$ where $E_k$ is the elastic modulus and

651    $\varepsilon_k^e$ is the elastic deformation of the wall. Let $l_k$ be the length of segment $k$, the rate of change

652    of $\varepsilon_k^e$ is given by:

$$\frac{\mathrm{d}\varepsilon_k^e}{\mathrm{d}t} + \Phi_k^w E_k \max\left(0, \varepsilon_k^e - \varepsilon_k^Y\right) = \frac{1}{l_k}\frac{\mathrm{d}l_k}{\mathrm{d}t}$$

654    where $\Phi_k^w$ is the extensibility and $\varepsilon_k^Y$ is the yield deformation of segment $k$. Equivalently, we

655    could define a yield stress.

656    *Mechanical equilibrium.* Let $P_i$ be the turgor pressure in each cell $i$. The tissue being at every

657    moment in a quasi-static equilibrium, pressure forces on wall edges and elastic forces within

658    walls balance exactly at each vertex $v$:

$$\frac{1}{2}\sum_{k \in f(v)} \Delta_k P A_k \boldsymbol{n}_k + \sum_{k \in f(v)} E_k \varepsilon_k^e a_k \boldsymbol{e}_{k,v} = 0$$

660    Where $f(v)$ is the set of walls adjacent to junction $v$, and $\Delta_k P = P_{k_1} - P_{k_2}$ is the pressure jump

661    across wall face $k$, with $k_1 < k_2$ as indices of the cells separated by face $k$, $A_k = h l_k$ is the area

662    of the face $k$ on which pressure is exerted, $\boldsymbol{n}_k$ is the normal vector to face $k$, oriented from cell

663    $k_1$ to cell $k_2$, and $a_k = hw$ is the cross-section of the face, on which the elastic stress is exerted;

25

664   finally, $\boldsymbol{e}_{k,v}$ is the unit vector in the direction of face $k$, oriented from junction $v$ to the other end

665   of face $k$. In the case of a single cylindrical cell for which growth is restricted to its principal

666   direction, the model is equivalent to the Lockhart-Ortega model.

667   *Fluxes.* For each cell $i$, the apoplasmic pathway is represented as a flux $U_i^a$ (in volume per

668   time unit) from the apoplast of constant water potential $\Psi^a$ through a perfectly semi-permeable

669   membrane: $U_i^a = A_i L_i^a (\Delta\Pi - P_i)$, where $A_i$ is the area of each cell in contact with the apoplast,

670   $L_i^a$ is the corresponding water conductivity, $\Delta\Pi = \pi_i + \Psi^a$ is assumed constant, and $\pi_i$ is the

671   osmotic pressure of cell $i$.

672   The symplasmic pathway corresponds to flows that occur through plasmodesmata, channels

673   between cells that convey both water and solutes. The symplasmic flows thus only depend on

674   turgor pressure difference. Let $L_{ij}$ be the symplasmic water conductivity corresponding to the

675   interface between two neighbour cells $i$ and $j$, and $A_{ij}$ their contact area, both assumed

676   symmetric: $L_{ij} = L_{ji}$ and $A_{ij} = A_{ji}$. The symplasmic flux $U_{ji}^s$ (in volume per time unit) from

677   cell $j$ to $i$ is defined by:

678   $$U_{ji}^s = A_{ij} L_{ij}^s (P_j - P_i)$$

679   Finally, the total water flux for cell $i$ is the sum of the apoplasmic flux $U_i^a$ and the symplasmic

680   fluxes $U_{ji}^s$ with all its neighbors, so that its volume variation can be expressed as:

681   $$\frac{\mathrm{d}V_i}{\mathrm{d}t} = A_i L_i^a (\Delta\Pi - P_i) + \sum_{j \in n(i)} A_{ij} L_{ij}^s (P_j - P_i)$$

682   where $n(i)$ is the set of neighbours of cell $i$.

683   *Cell division.* We implemented the Willis-Refahi rule [34], in which the division volume is

684   given by $V_0 = f V_b + \mu_b (2 - f + Z)$, where $f = 0.5$, $V_b$ is the volume at birth, $\mu_b = 3.31$

685   is the mean birth volume and $Z$ is a Gaussian noise with zero mean and $\left(4\sigma_d^2 - f^2\sigma_b^2\right)^{1/2}$

686   standard deviation, with $\sigma_b = 0.2$ and $\sigma_d = 0.1$.

687   *Numerical resolution.* In the Lockhart-Ortega model, the compatibility between wall elongation

26

688   and cell volume increase is automatically enforced through the geometrical constraint of

689   unidirectional growth that leads to equal relative growth rate of the cell and strain rate of the

690   walls. In our multicellular model, this equality is no longer true. Instead, the lengths $l(X)$ of the

691   edges and the volumes $V(X)$ of the cells are expressed as functions of the positions $X$ of the

692   vertices; then, given an initial position $X$ of the vertices and elastic deformation $\varepsilon^e$ of the edges,

693   the equations of wall rheology, mechanical equilibrium, and water fluxes form a closed set of

694   equations with respect to the unknowns $X$, $P$, and $\varepsilon^e$ that allow to predict their evolution.

695   To give an idea of the mathematical complexity of the problem, one may consider the following

696   example: in a connected tissue, if one cell is stretched and forced to increase its volume, an

697   equal volume of water has to enter the cell, either from the apoplastic compartment or the

698   neighbour cells. In the latter case, pressure should drop in the neighbour cells, which should

699   attract water from their own neighbours, and this could propagate to further cells depending on

700   the geometry of the tissue and the effective parameters. Volume and therefore positions of the

701   vertices could be also affected. Finally, one can see that the interaction between hydraulics and

702   mechanics implies long range interactions where pressure plays a key role.

703   We developed an original algorithm and implemented it in an in-house code, where at each time

704   step, the mechanical equilibrium is resolved under constraints on the cell volume (from the

705   water fluxes), and constraints on the cells edges (from the rheological law of the walls). This

706   was implemented in Python, using the open source libraries NumPy, SciPy, and the Topomesh

707   class          from          the          OpenAlea          project

708   (http://openalea.gforge.inria.fr/doc/vplants/container/doc/html/container/openalea_container_t

709   opomesh_ref.html). This algorithm is described in more detail in a separate publication [30].

710   The computations were run on a computer with a 3.6GHz Intel Xeon E5 processor, 64 GB of

711   RAM, and running Linux Debian Stretch. The typical computing time was one week for each

712   computation.

713   *Parameterization of the model.* The reference values of the parameters were chosen based on

714   the literature or on our experiments (main text Table 1), except for $\alpha^s$, for which no data is

715   available and was conservatively ascribed an intermediate value of 0.5. Model behaviour was

27

716     explored by changing non-dimensional parameter values as explained in the main text.

717     *Procedure for the computations.* We first run in parallel three computations with cell division

718     to around 300 cells. To mimic untreated case, simulations continue until around 600 cells. To

719     mimic the oryzalin treatment, the current states of the "untreated" computations at around 300

720     cells are used as initial conditions for the oryzalin case: division is stopped, and we run

721     computations either with the same effective parameters, or with some parameters modified so

722     that the behaviour of the oryzalin treated meristems is recovered (see supplementary table 2);

723     the computations are run until the total volume has been multiplied by three from this initial

724     state. Typical runtime for one parameter set is one week.

| Dividing simulations | SIM# | $n$ | Non-dividing simulations | SIM# | $n$ |
|---|---|---|---|---|---|
| Initial (Fig. 1f) $\alpha^s = 0.5$, $\alpha^a = 0.5$, $\theta = 7/3$ | 3 | 1535 | No division (Fig. 1h, 6d) | 3 | 759 |
| Reference (Fig. 1g, 6a) $\alpha^s = 0.5$, $\alpha^a = 0.5$, $\theta = 20/3$ | 3 | 1496 | $\Delta\Pi \times 2$ | 3 | 759 |
| $\theta = 10/3$ | 3 | 1515 | $w \times 2$ | 3 | 759 |
| $\theta = 10$ | 3 | 1519 | $w \times 4$ (Fig. 6g) | 3 | 759 |
| $\theta = 40/3$ | 3 | 1530 | $\Delta\Pi \times 2$, $w \times 2$ | 3 | 759 |
| $\alpha^s = 0.1$ | 3 | 1506 | $\Delta\Pi \times 2$, $w \times 4$ | 3 | 759 |
| $\alpha^s = 0.9$ | 3 | 1525 | | | |
| $\alpha^a = 0.1$ | 3 | 1507 | | | |
| $\alpha^a = 0.9$ | 3 | 1519 | | | |

725     **Supplementary table 2. Parameter modification and simulation repeats.** Parameters are

726     systemically changed, with the reference parameter set $\alpha^s = 0.5$, $\alpha^a = 0.5$, $\theta = 20/3$ for

727     exploration in untreated simulations and for mimicking oryzalin in non-dividing simulations.

728     Annotations are as described above. SIM#, number of simulations; *n*, total cell number at last

729     time point without boundary cells.

730     **Acknowledgements**

28

**Author contributions**

743 This study was initiated by A.B. Y.L. and A.B. designed the experiments. Y.L. executed AFM

744 and confocal microscopy, acquired experimental data except EM, and analysed experimental

745 and simulation data. J.T. performed electron microscopy. V.M and M.D. wrote scripts to

746 facilitate experimental data analysis. I.C. and C.G. designed physical model of tissue growth.

747 I.C. implemented the model, ran simulations, optimized model parameters and analysed

748 simulation data. G.M. designed, ran, and analysed indentation simulations. Y.L. and A.B.

749 contributed to the design of simulations. Y.L., I.C., V.M., G.M., C.G. and A.B. contributed to

750 data interpretation. Y.L. and A.B. wrote the manuscript with inputs from the other authors.

**Data availability**

752 All materials, scripts and datasets generated and analysed during the current study are available

753 from the corresponding authors upon reasonable request.

754 **Figures**
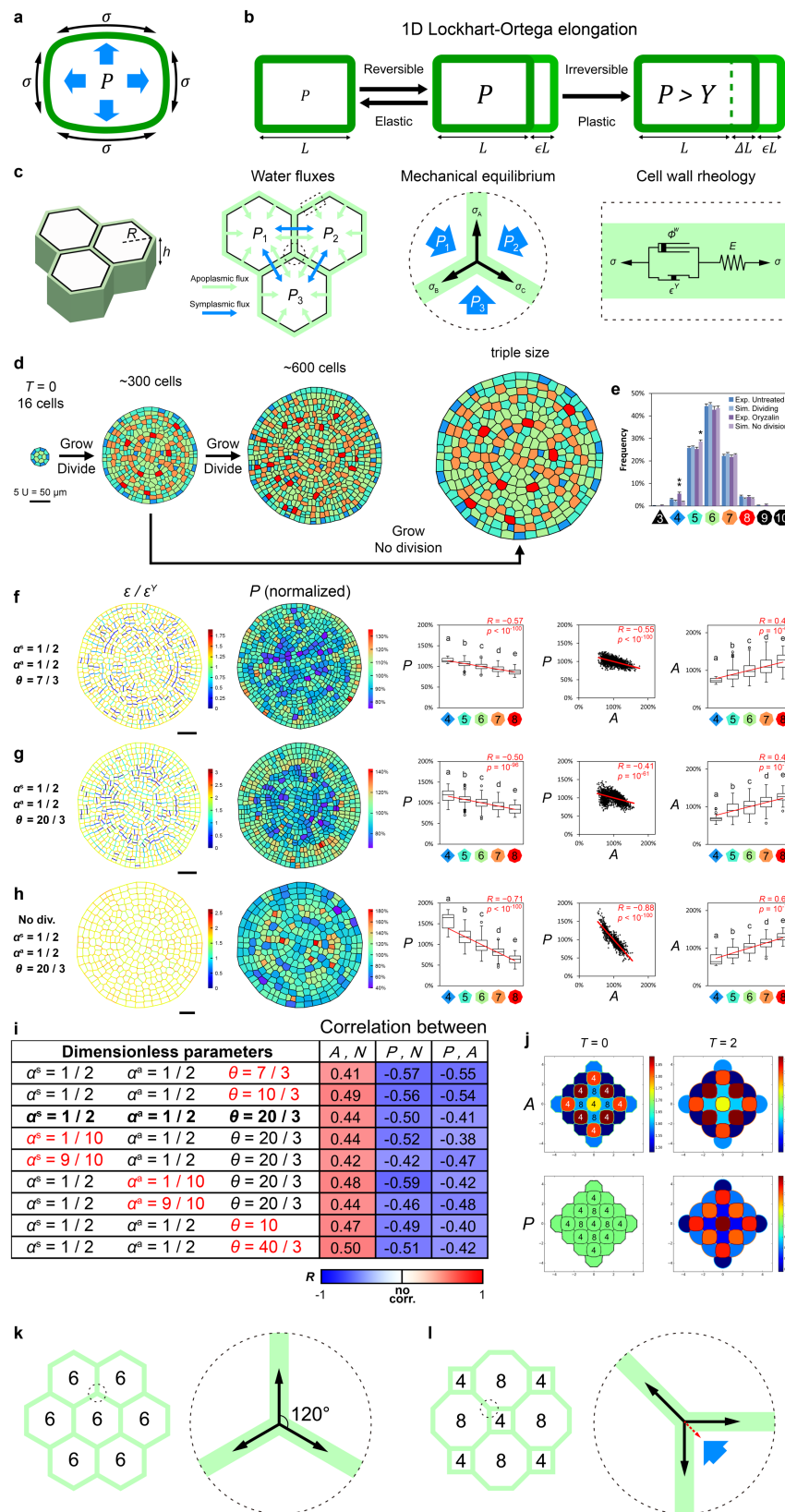


**Figure 1. Turgor pressure heterogeneity emerges from cell topology in the mechano-hydraulic model.**

(**a**) In a plant cell, the turgor pressure $P$ is contained by the cell wall tensile stress $\sigma$. (**b**) A schematic representation of the Lockhart-Ortega equation, where 1D cell length $L$ elongation is a combination of reversible stretch $\epsilon L$ (elasticity, $\epsilon$ is elastic strain) and cell wall yield $\Delta L$ at longer timescale (viscosity) if $P$ is higher than a threshold $Y$ (effective plasticity, $\Delta L = \Phi t L (P - Y)$, $\Phi$ is wall extensibility, $t$ is time). (**c**) Schematic representations of model components, including cell geometry with height $h$ and radius $R$ (left), apoplasmic/transmembrane and symplasmic/intercellular water fluxes (middle left), mechanical equilibrium at tricellular junctions (middle right) and the visco-elasto-plastic cell wall rheology (right). $P_i$, cell-specific turgor pressure; $\sigma$, cell wall tension; $\Phi^w$, wall extensibility; $\varepsilon^Y$, wall strain threshold; $E$, wall Young's modulus. (**d**) Simulation snapshots: in "dividing" simulations, 16 initial cells grow and divide until about 600 cells; in "non-dividing" simulations, divisions are stopped when cell number reaches about 300 cells and growth continues until they triple in size. Colour indicates cell neighbour number as in (e). (**e**) Similar distributions of cell neighbour number in the experimentally observed (Exp.) shoot apical meristem and in simulations (Sim.) by Kolmogorov–Smirnov test (confidence level $\alpha = 0.05$, $D_{n,m} < D_\alpha$), error bars are standard deviations. *, Student's $t$-test $p < 0.05$; **, $p < 0.01$. (**f-h**) Cell wall strain, turgor pressure, neighbour number, and area in dividing (f, g) and non-dividing (h) simulations; the dimensionless parameter for flux-wall balance $\alpha^a$, apoplasmic-symplasmic balance $\alpha^s$ and the osmotic drive are as indicated. Left: cell wall elastic strain $\varepsilon$ normalized by yield strain $\varepsilon^Y$; middle left: cell turgor pressure $P$ normalized by average pressure; middle: boxplots of normalized cellular turgor pressure $P$ against cell topology $N$ (**f**, $n = 1535$ cells; **g**, $n = 1496$ cells; **h**, $n = 759$ cells); middle right: normalized pressure against normalized area; right: normalized area against neighbour number. Cells on the mesh edge were not analysed due to border effect. Circles are Tukey's outliers; lowercase letters indicate statistically different populations (Student's $t$-test, $p < 0.05$); red lines indicate linear regressions, with Pearson correlation coefficient $R$ and corresponding $p$-value. In (**d, f-h**) scale bars are 5 unit length. (**i**) Model parameter exploration. Colours indicate Person correlation coefficient $R$, with perfect anticorrelation as blue ($R = -1$), perfect correlation in red ($R = 1$); all correlations were statistically significant ($p < 0.05$). $A$, normalized cell area; $N$, cell neighbour number; $P$, normalized turgor pressure; $\alpha^a$, dimensionless parameter for flux-wall balance; $\alpha^s$, dimensionless parameter for apoplasmic-symplasmic balance; $\theta$, dimensionless osmotic drive. (**j**) Simulations initiated with 4-edged bigger than 8-edged cells, shown at two simulation times, with area and pressure shown in top and bottom, respectively; 4-edged cells have higher pressure although bigger. (**k** to **l**) Schematic explanation of topology-derived turgor pressure heterogeneity. (**k**) Three-cell junctions in a tissue of hexagonal cells are at mechanical equilibrium with equal tensions and equal wall-wall angles. (**l**) Fewer-neighboured cells have sharper wall-wall angles, a tension that is roughly constant per wall effectively results in mechanical compression due to unequal projected tension distribution (red dash-line arrow) that is balanced by higher turgor pressure build-up (big blue arrow).
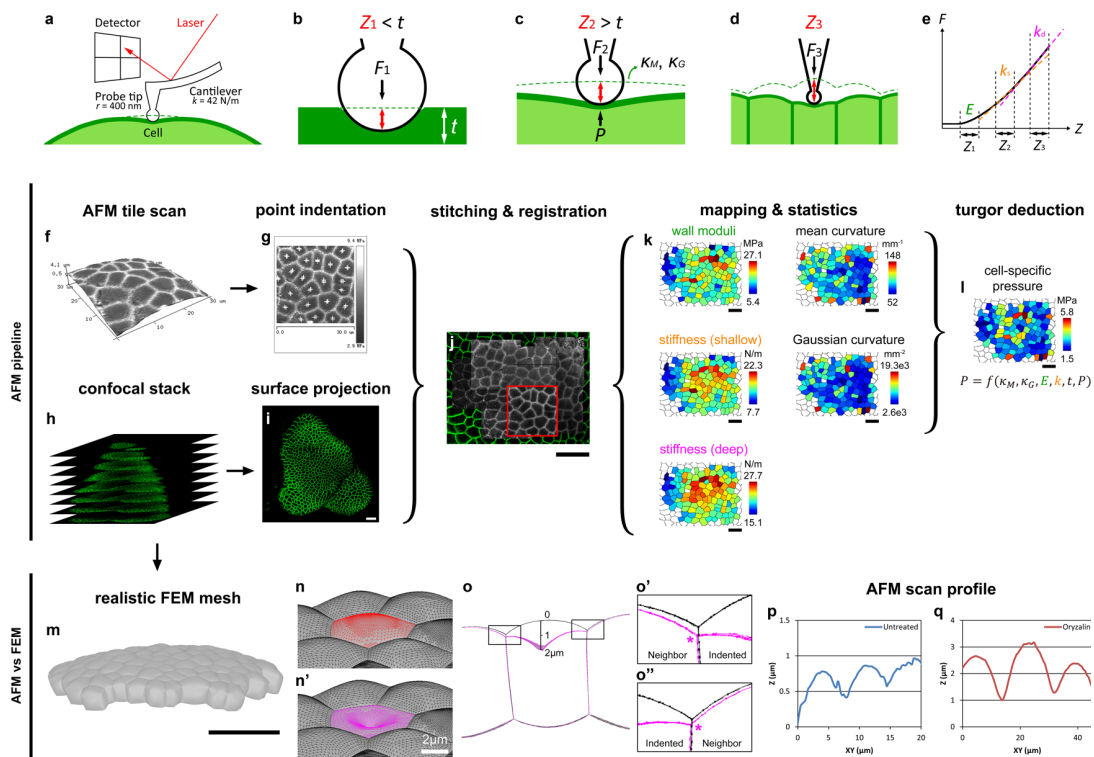
**Figure 2. The experimental pipeline for turgor pressure deduction.**

(**a**) Schematic representation of AFM nanoindentation for turgor pressure measurement. $r$, probe tip radius; $k$, cantilever stiffness. (**b** to **e**) Illustration for force curve interpretation at different indentation depth. (b) When indentation depth $Z_1$ is smaller than wall thickness $t$, the force-indentation curve is sensitive to cell wall property, (c) deeper-than-wall indentation $Z_2 > t$ is also sensitive to turgor pressure $P$. (d) Even deeper indentation $Z_3$ deforms surrounding cells and is also sensitive to tissue context. Dotted line marks the shell position before indentation, which is used to determine surface mean and Gaussian curvature, $\kappa_M$ and $\kappa_G$, by AFM topographic scan. (e) Three regimes of the force-indentation curve are used to fit for cell wall Young's modulus $E$, apparent stiffness at cell-scale $k_s$ and tissue scale $k_d$. $F$ denotes indentation force. (**f** to **l**) The AFM-confocal pipeline of measurement and deduction on an example untreated SAM. (f) Derjaguin-Muller-Toporov (DMT) modulus map, highlighting cell contours, is projected on the surface topography of an AFM scan. Smaller scan region is chosen to bypass the SAM surface unevenness. (g) Multiple indentations (marked by crosshair) are performed near the barycentre of each cell. (h and i) Confocal stack and its surface projection of the same SAM with plasma membrane GFP signal. (j) Tiled AFM scans are overlaid and stitched on the confocal surface projection image, red square marking the same tile from (f and g). Individual indentation positions are registered on a global coordinate and assigned to segmented cells. (k) Force curves are analysed, and the cellular average of physical values are mapped. (l) Turgor pressure is deduced per force curve and averaged per cell. Stiffness from very deep indentation is not used for cell-specific deduction. (**m** to **o''**) Virtual indentation on realistic 3D mesh. (m) The epidermal layer is meshed based on confocal image. Cells are pressurized with a uniform 2 MPa turgor pressure. (n and n') A cell before (red) and being indented (magenta). (o to o'') Longitudinal section of the indented mesh; black, before indentation; magenta, being indented. Cell junctions

(rectangles) are magnified to highlight the neighbour cell deformation (marked by asterisks) by very deep indentation. (**p** and **q**) AFM-determined surface profiles of untreated (p) and oryzalin-treated SAM (q). Scale bars represent 20 μm if not specified. Note that z axes in (f, p and q) are stretched to emphasize SAM surface unevenness.
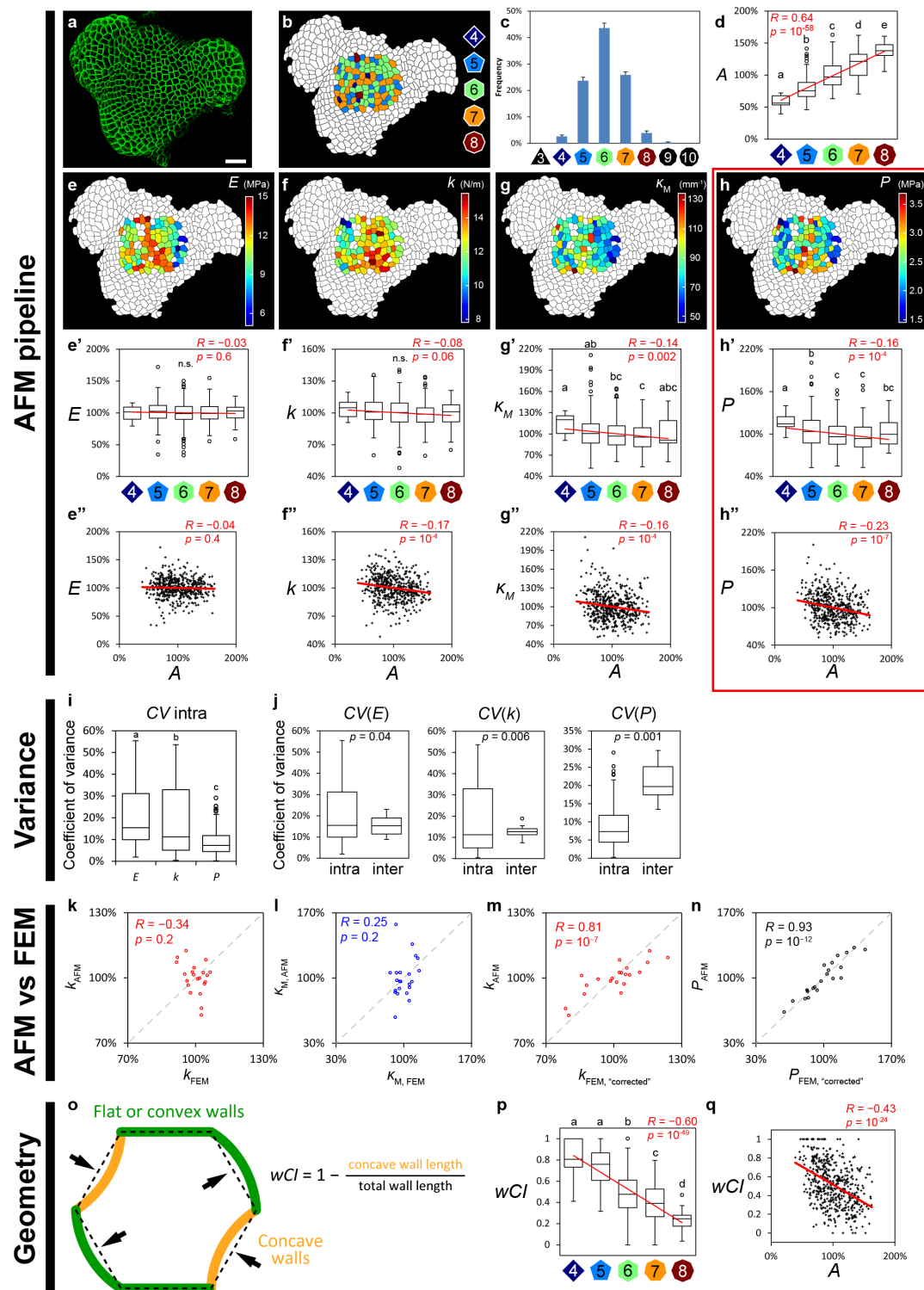


**Figure 3. Turgor pressure heterogeneity in untreated SAM.**

(**a**) Top-view surface projections of untreated SAM with plasma membrane GFP signal; scale bars represent 20 μm. (**b**) Map of epidermal cell neighbour number. (**c**) Distribution of neighbour number on 7 untreated SAM surfaces, error bars are standard errors of means. (**d**) Normalized cell area $A$ and cell neighbour number $N$ are linearly correlated. (**e** to **h"**) AFM-determined cellular values and their association with neighbour number $N$ and cell area $A$, all plotted values are normalized per SAM (7 SAMs, $n = 503$ cells). (e to e'') Cell wall Young's moduli $E$, (f to f'') apparent stiffness $k$ at intermediate indentation depth, (g to g'') cell surface mean curvature $\kappa_M$, (h to h'') deduced turgor pressure $P$. (**i** and **j**) Coefficient of variance (CV) of AFM-determined values in untreated meristems. (i) At subcellular scale (intra), $P$ is much less variable than $E$ and $k$. (j) $P$, unlike $E$ and $k$, are more heterogeneous between cells (inter) than between measurements within single cells (intra). (**o** to **q**) Weighed convex index (wCI) anticorrelates with cell neighbour number (p) and normalized cell area (q). In box plots, circles are Tukey's outliers; lowercase letters indicate statistically different populations (Student's $t$-test, $p < 0.05$); red lines indicate linear regressions, with Pearson correlation coefficient $R$ and corresponding $p$-value.
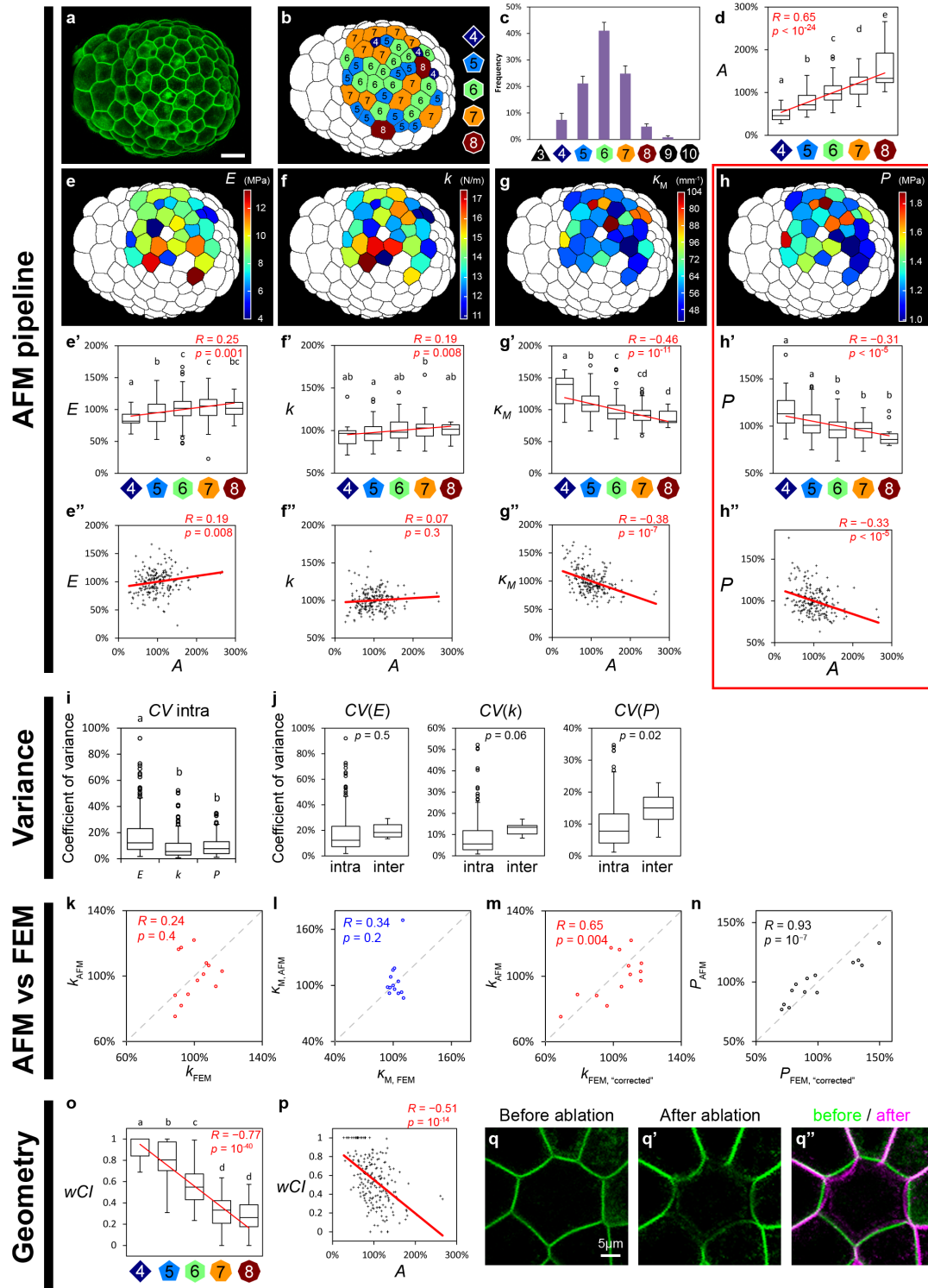
**Figure 4. Turgor pressure heterogeneity in oryzalin-treated SAM.**

(**c**) Top-view surface projections of oryzalin SAM with plasma membrane GFP signal; scale bars represent 20 μm. (**b**) Map of epidermal cell neighbour number. (**c**) Distribution of neighbour number on 9 untreated SAM surfaces, error bars are standard errors of means. (**d**) Normalized cell area $A$ and cell neighbour number $N$ are linearly correlated. (**e** to **h"**) AFM-determined cellular values and their association with neighbour number $N$ and cell area $A$, all plotted values are normalized per SAM (9 SAMs, $n$ = 202 cells). (e to e") Cell wall

Young's moduli $E$, (f to f'') apparent stiffness $k$ at intermediate indentation depth, (g to g'') cell surface mean curvature $\kappa_M$, (h to h'') deduced turgor pressure $P$. (**i** and **j**) Coefficient of variance (CV) of AFM-determined values in untreated meristems. (i) At subcellular scale (intra), $P$ and $k$ are much less variable than $E$. (j) $P$ and $k$, unlike $E$, are more heterogeneous between cells (inter) than between measurements within single cells (intra). (**o** to **q''**) Weighed convex index (wCI) anticorrelates with cell neighbour number (o) and normalized cell area (p). (q to q'') Cell walls curve towards cell with low pressure, as signified by the enhanced curvature towards the ablated cell with released pressure. In box plots, circles are Tukey's outliers; lowercase letters indicate statistically different populations (Student's *t*-test, $p < 0.05$); red lines indicate linear regressions, with Pearson correlation coefficient $R$ and corresponding *p*-value.
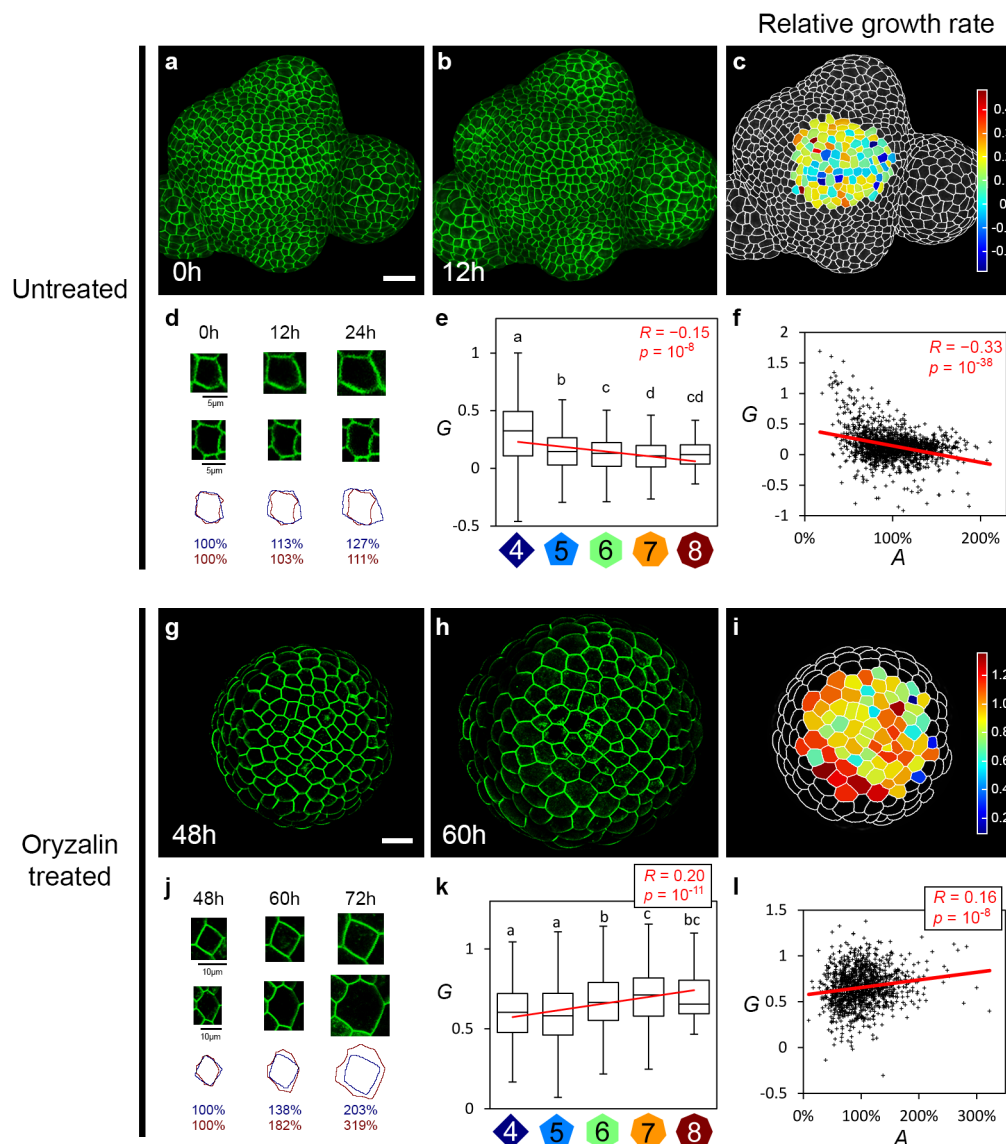


**Figure 5. Cellular growth rate bifurcates between conditions.**
(**a** to **f**) Relative growth rate per day $G$ of untreated SAM cells. (**g** to **l**) Cellular growth rate per day of oryzalin-treated SAM between 12-hour interval (48 and 60 hours post treatment). (a, b, g and h) Surface projections of untreated or oryzalin-treated SAM at initial time point

36

(a and g) and 12 hours later (b and h); scale bars are 20 μm unless otherwise noted. (c and i) Heat maps of areal relative growth rate per day. (d and j) Example 4 and 8-neighbored cells during 24-hour growth, with areal normalization at initial time point. Cell contour and relative size (blue for 4-neighbored, red for 8-neighbored) depict the diverging growth trends. Scale bars are as indicated. (e, f, k and l) Box plots of relative growth rate per day $G$ against cell topology $N$ (e and k) and dot plots of relative growth rate per day $G$ against normalized cell area $A$ (f and l) (e and f, untreated 11 SAMs, $n = 1491$ cells; k and l, oryzalin-treated 14 SAMs, $n = 1160$ cells). Note that Tukey's outliers are plotted in Figure S5 and all data are included for statistical analyses. Lowercase letters indicate statistically different populations (Student's $t$-test, $p < 0.05$); red lines indicate linear regressions, with Pearson correlation coefficient $R$ and corresponding $p$-value.
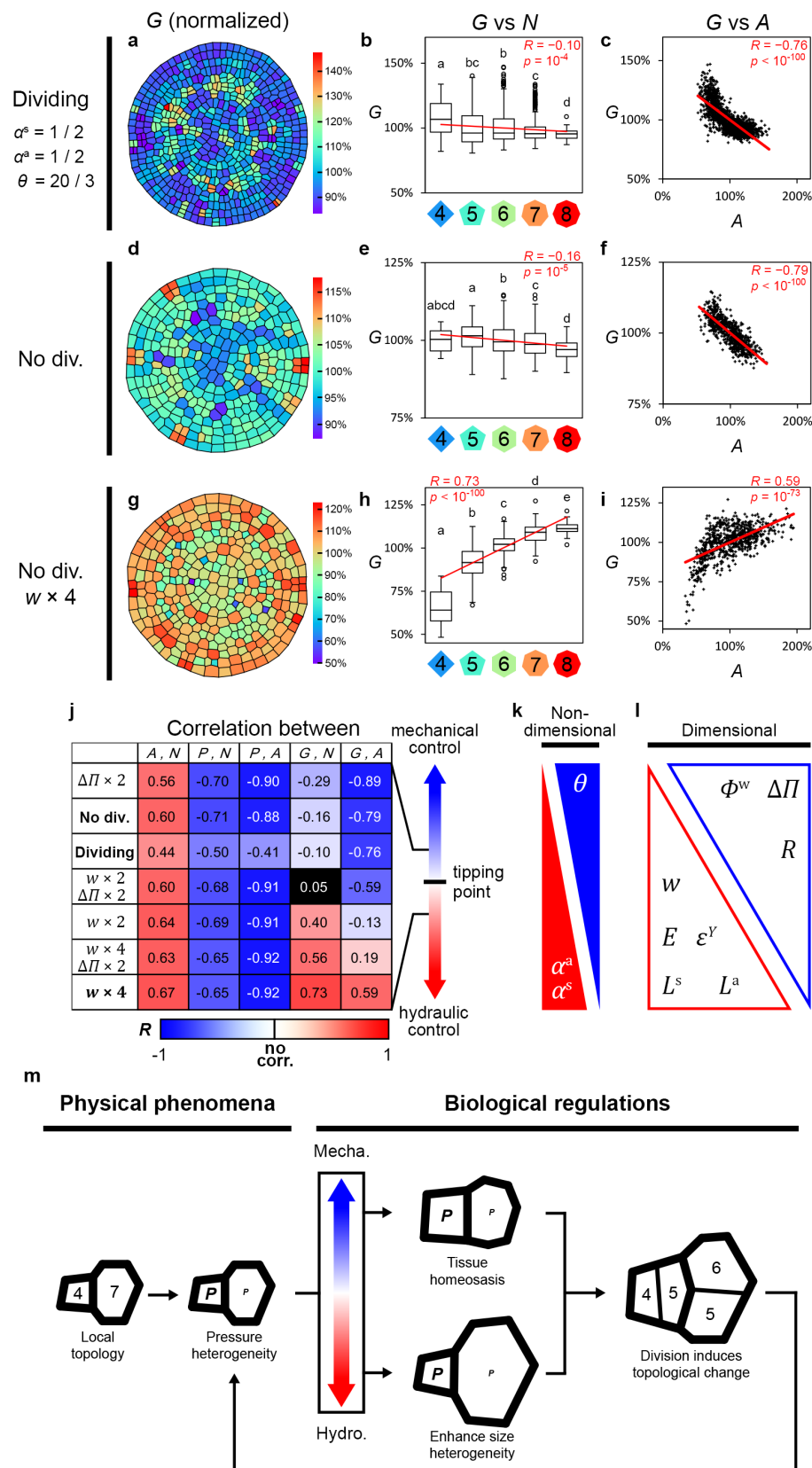
**Figure 6. The model recapitulates the untreated and oryzalin-treated growth trends.**
(**a** to **i**) Relative growth rate $G$ normalized by average growth rate, neighbour number $N$, and normalized cell area $A$, with reference values of dimensionless parameters ($\alpha^a = 0.5$, $\alpha^s = 0.5$,

$\theta$ = 20/3): dividing simulations (a-c), non-dividing simulations (d-f), and non-dividing simulations with quadruple wall thickness $w$ to mimic oryzalin treatment (g-i). (a, d, g) Heat maps of normalized areal relative growth rate. (b, e, h) Box plots of normalized relative growth rate $G$ against cell topology $N$. Lowercase letters indicate statistically different populations (Student's $t$-test, $p < 0.05$); red lines indicate linear regressions, with Pearson correlation coefficient $R$ and corresponding $p$-value. (c, f, i) Dot plots of normalized relative growth rate $G$ against normalized cell area $A$. For numbers of repeats see STAR Methods. (**j**) Model exploration to fit oryzalin-treated case. Colours indicate Person correlation $R$, with perfect anticorrelation as blue ($R$ = -1), perfect correlation in red ($R$ = 1), and insignificant correlation ($p > 0.05$) in black. $A$, normalized cell area; $N$, cell neighbour number; $P$, normalized turgor pressure; $G$, normalized relative growth rate; $\Delta\Pi$, transmembrane osmotic pressure difference; $w$, wall thickness. (**k, l**) Influence of dimensionless (k) and dimensional parameters (l) on growth trends. Triangles indicate parameter's influence to the mechanical–hydraulic balance. $\alpha^a$, dimensionless parameter for flux-wall balance; $\alpha^s$, dimensionless parameter for symplasmic-apoplasmic balance; $\theta$, dimensionless osmotic drive. $w$, wall thickness; $E$, cell wall modulus; $\varepsilon^Y$, strain threshold; $L^a$, cross-membrane water conductivity; $L^s$, cell-to-cell symplasmic conductivity; $\Phi^w$, wall extensibility; $\Delta\Pi$, transmembrane osmotic pressure difference; $R$, representative cell size. (**m**) Summary of growth trend inversion according to the mechanical–hydraulic control shown in (j). The wall and flux limits correspond to untreated and oryzalin-treated SAMs, respectively.
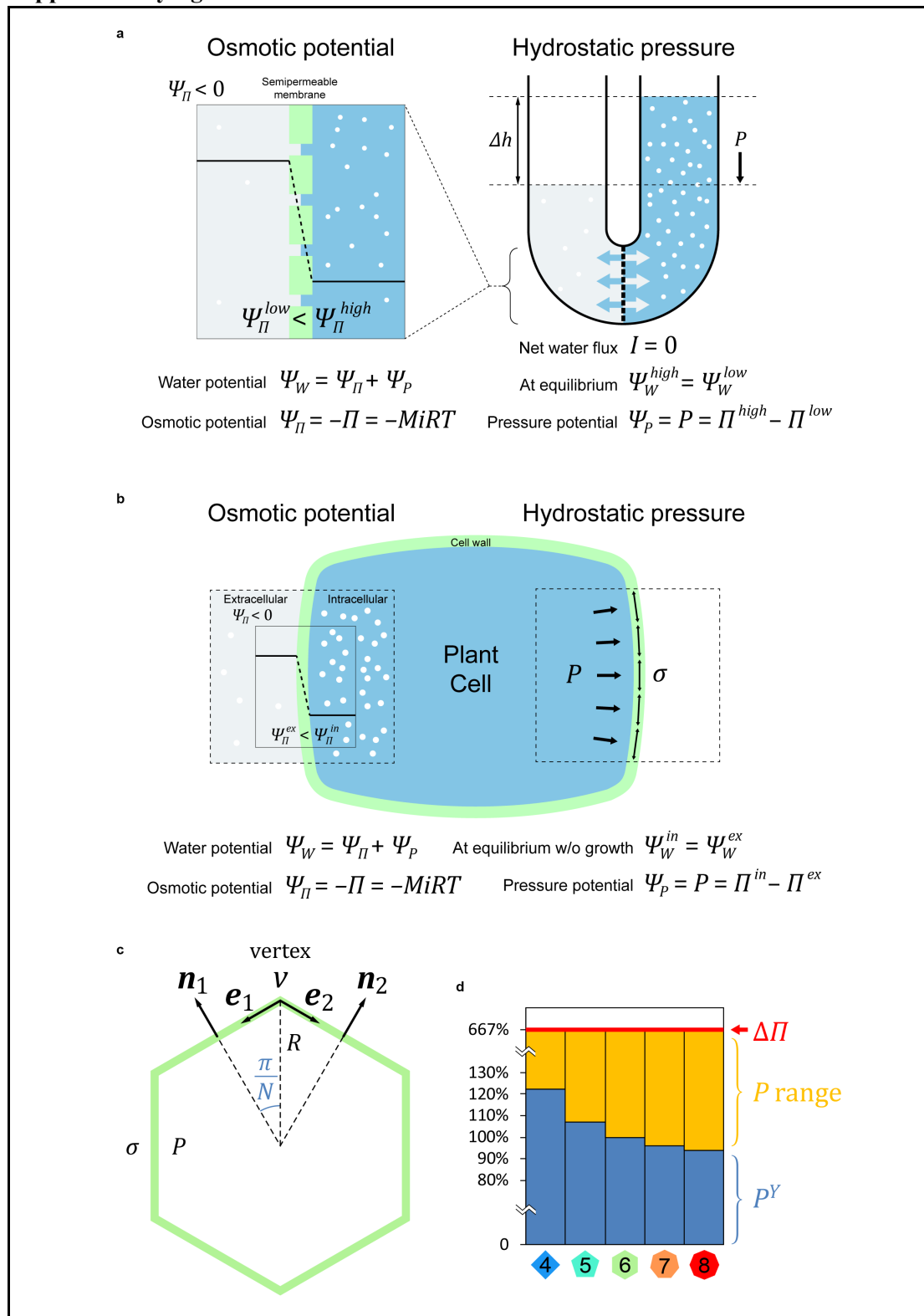
755

**Supplementary figures**



**Figure S1. Osmotic pressure and hydrostatic pressure.**

(**a**) Osmosis occurs when solutions of different osmotic pressure $\Pi$, due to different solute concentration (depicted by the density of white dots), are separated by a semipermeable membrane. Difference of osmotic potential $\Psi_\Pi$ (depicted by horizontal black lines, always negative in solutions) across the membrane dictates that solvent flows from high to low

potential compartment (low to high solute concentration). In a U-shaped tube setup (right), osmosis may stop before the two compartments reach the same concentration, as the extra volume (in fact height, $\Delta h$) in the higher-concentration compartment exerts a hydrostatic pressure $P$ due to gravity that pushes the solvent back. $P$ increases until reaching the same value as $\Delta\Pi$ at equilibrium where the total water potential $\Psi_W$ is equal on both sides, and the net solvent flux $I = 0$ (indicated by the opposite blue arrows). $M$, solute molar concentration; $i$, van t'Hoff index of solute that disassociates; $R$, ideal gas constant; $T$, absolute temperature. (**b**) Osmosis in a plant cell, where gravity is neglected for its small size. Because of the rigid cell wall that restricts the cell volume, hydrostatic pressure $P$, alias turgor pressure, builds up alongside cell wall tension $\sigma$ to counterbalance the difference of osmotic potential $\Psi_\Pi$, until $P = \Delta\Pi$. (**c**) Geometrical extension of Lockhart model for a single polygonal cell. $\sigma$, cell wall stress; $P$, turgor pressure; $R$, cell radius; $N$, polygon class; v, vertex; $\boldsymbol{n_1}$ and $\boldsymbol{n_2}$; normal vector; $\boldsymbol{e_1}$ and $\boldsymbol{e_2}$, tangent vector. (**d**) Half of the threshold pressure of a polygonal cells base on $P^Y = \dfrac{w}{2R\cos(\pi/N)} E\varepsilon^Y$. For growing cells, turgor pressure $P$ falls between the transmembrane osmotic pressure $\Delta\Pi$ and pressure threshold $P^Y$.
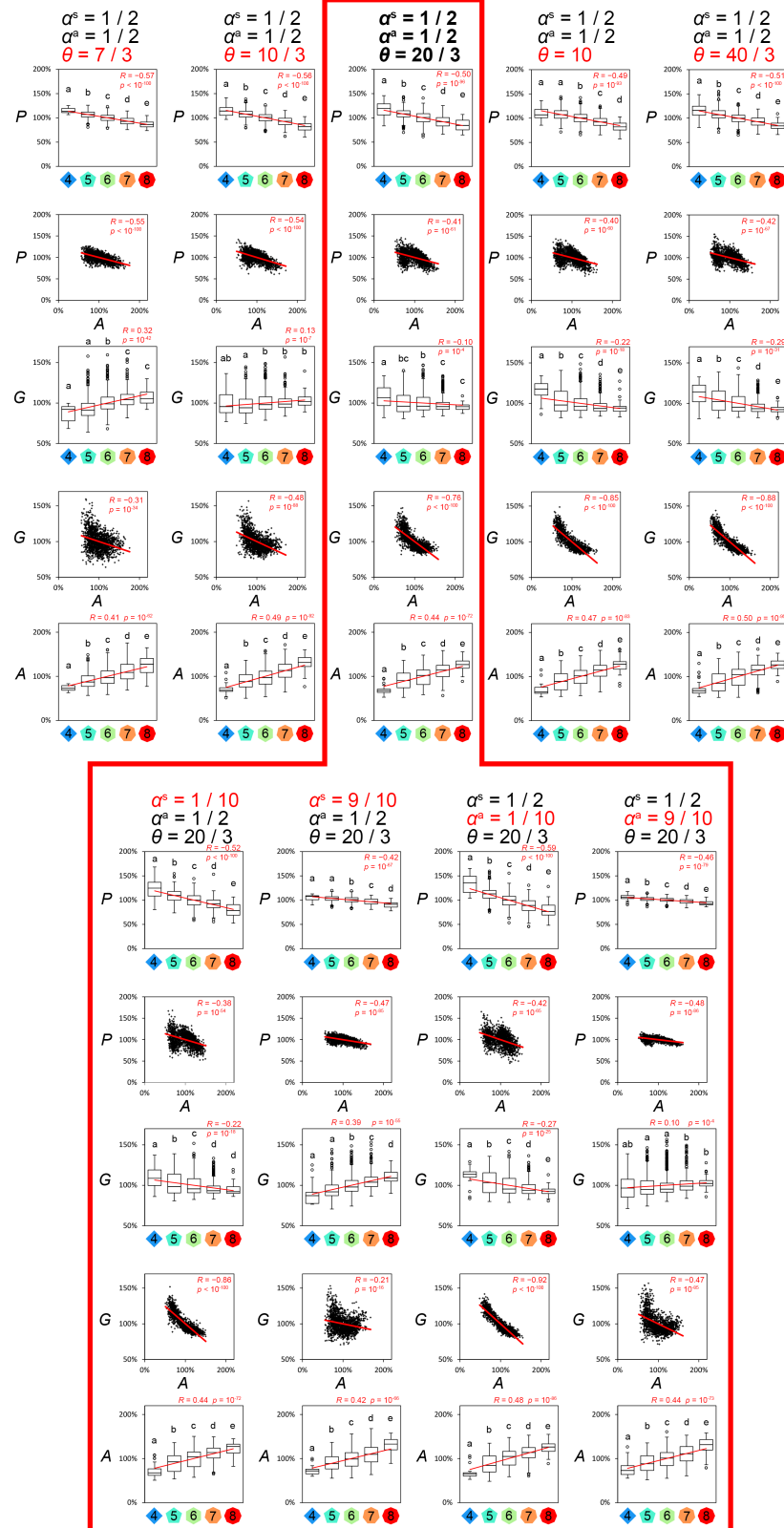
41

**Figure S2. Simulations for vertex model parameter exploration.**

Model parameters were systemically changed. $\alpha_a$, dimensionless parameter determining the weight of the limitation of growth by transmembrane permeability to the combined limitation of growth by cell wall extensibility and transmembrane permeability; $\alpha_s$, dimensionless

parameter determining the weight of intercellular water conductivity over total (intercellular and transmembrane) conductivity; $s$, cell size scale at division relative to the initial setting. $P$, normalized turgor pressure, $A$, normalized cell area; $G$, relative growth rate per hour. Polygons indicate cell neighbour number. Red lines indicate linear regressions, with Pearson correlation coefficient $R$ and corresponding $p$-value.
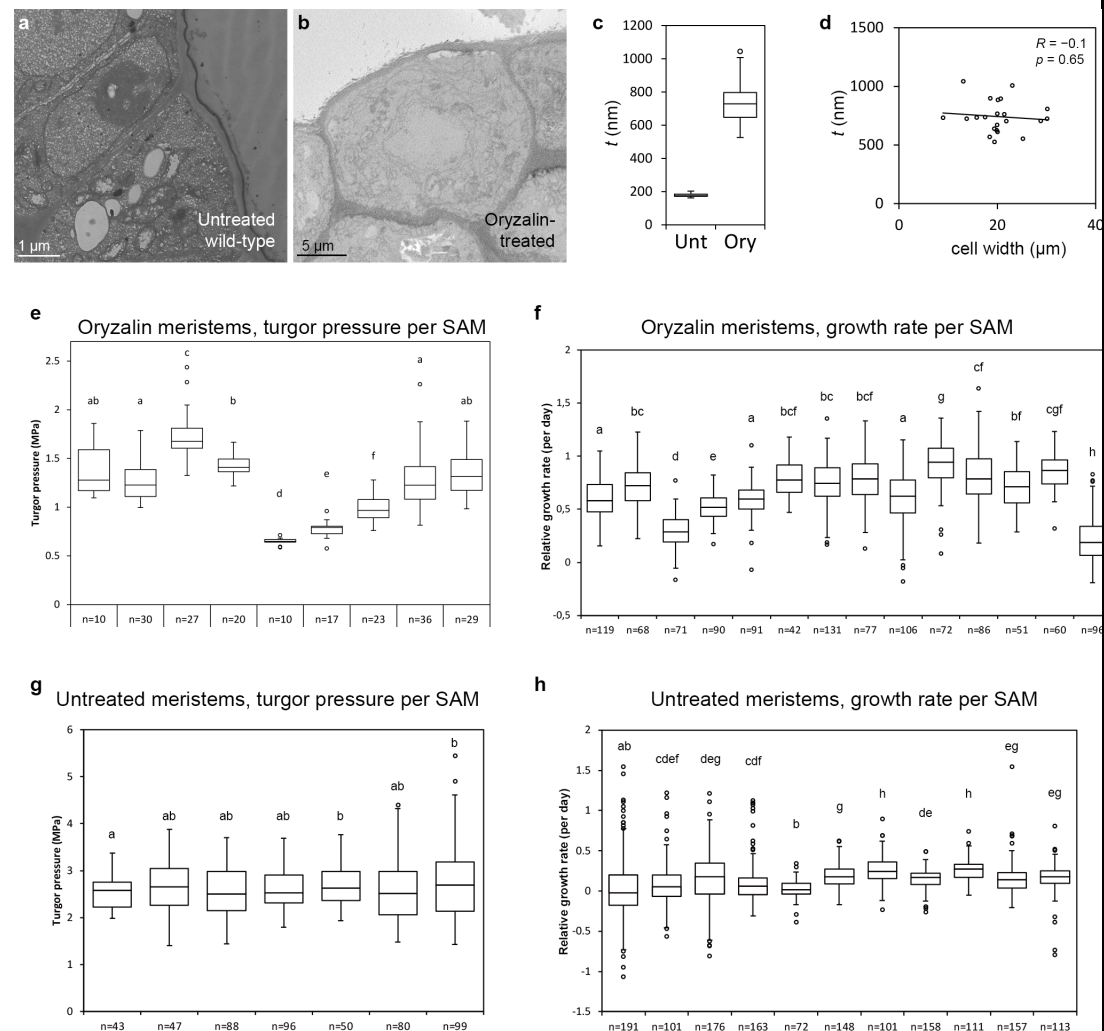


**Figure S3. Cell wall thickness and individual SAM measurements of turgor pressure and growth rate.**

(**a** and **b**) TEM and serial block-face imaging SEM images of untreated (a) and oryzalin-treated meristem (b). (**c**) Boxplots of surface wall thickness of untreated (Unt) and oryzalin-treated (Ory) meristems. (**d**) Surface wall thickness does not correlate to cell width in oryzalin-treated meristems. (**e-h**) Oryzalin-treated SAMs showed highly variable turgor pressure and growth rate per SAM, while untreated samples show little variation; $n$ is cell number measured per meristem. Circles are Tukey's outliers; lowercase letters indicate statistically different populations (Student's $t$-test, $p < 0.05$). (g) The first five untreated meristems measured by AFM were of ecotype WS-4, while the last two are of Col-0.
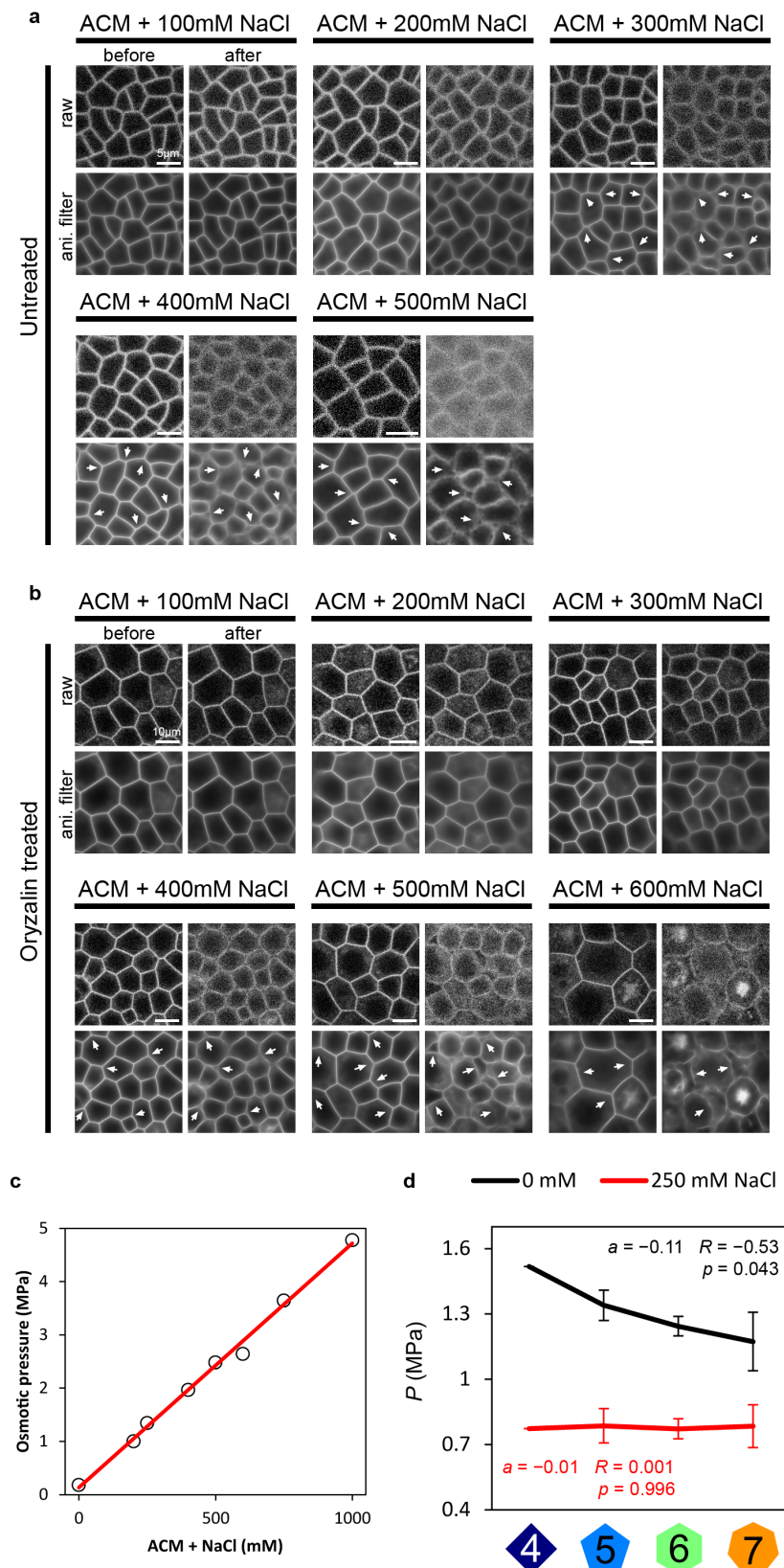
**Figure S4. Hyperosmotic treatments on SAMs.**

(**a** and **b**) Confocal images of untreated (a) and oryzalin-treated (b) meristems submerged in liquid apex culture medium (ACM) before and after the supplementation of NaCl. The

increased osmolality resulted in blurred images (each upper-right subpanel), possibly due to altered refraction limit, which required anisotropic filtering to enhance the trajectory of cell contours. Out of 8 untreated meristems, half showed incipient plasmolysis at 200 mM NaCl (~0.4 Osm) and the other half at 300 mM (~0.6 Osm). For 7 oryzalin-treated meristems, incipient plasmolysis occurred among a broader osmolarity (2 meristems at 300 mM, 3 meristems at 400 mM, 2 meristems at 500 mM). Arrows points to noticeable membrane detachment and rounding, indicating plasmolysis. (**c**) Osmolarity calibration by osmometer measurements ($r^2 > 0.99$). (**d**) Moderate hyperosmotic treatment decreases AFM-determined turgor pressure, and reduces turgor heterogeneity plotted against cell neighbour number (linear regression slope $a$, Pearson correlation coefficient $R$ and corresponding $p$-value).
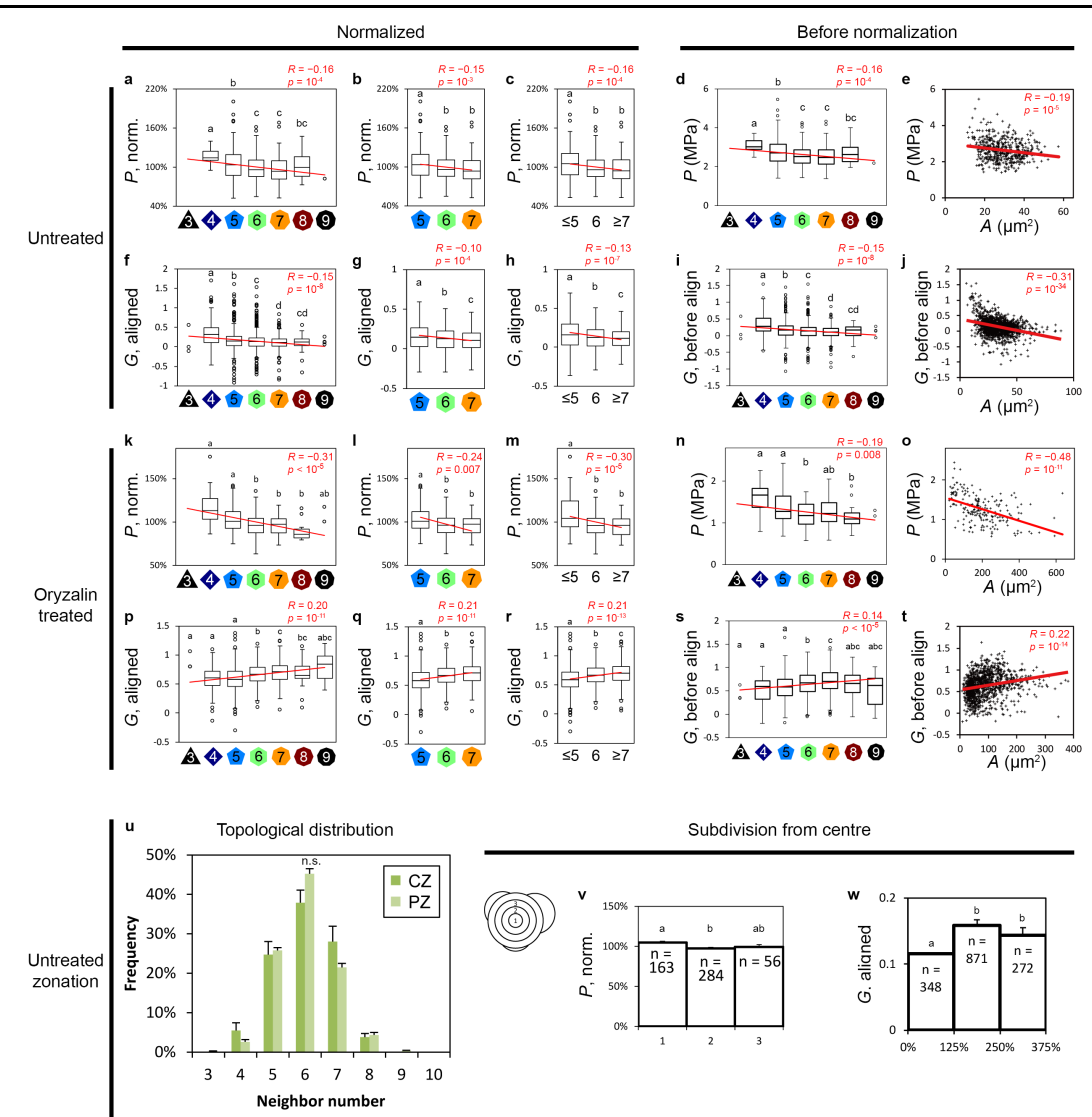


**Figure S5. Pressure and growth rate before and after normalization, and regional measurements.**

(**a** to **j**) Normalized and raw turgor pressure $P$ and growth rate $G$ of untreated meristems plotted against cell neighbour number $N$ and cell area $A$. (**k** to **t**) Normalized and raw turgor pressure $P$ and growth rate $G$ of oryzalin-treated meristems plotted against cell neighbour number and cell area. (a, f, k, p) Normalized $P$ and co-aligned $G$ against $N$ plots complete

with outliers and the rare 3- and 9-neighboured cells, same data as in Figure 3 and 4. (b, g, l, q) Same normalized data with only the major polygonal classes ($N = 5, 6, 7$), showing that the correlations do not depend on the rare polygonal classes at the ends of distributions. (c, h, m, r) Same normalized data were binned for cells with 5 or fewer neighbours ($\leq 5$), cells with 6 neighbours and cells with 7 or more neighbours ($\geq 7$), showing the same trends as unbinned data. (d, i, n, s) Raw data of $P$ and $G$ before normalization / co-alignment against neighbour number; (e, j, o, t) raw data of $P$ and $G$ before normalization / co-alignment against unnormalized cell area, all showing the same trend as normalized data. Red lines are linear regression line, with Pearson correlation coefficient $R$ and corresponding $p$-value. Lower case letters denote statistically significant groups (Student's $t$-test $p < 0.05$). (**u**) Frequency of $N$-neighboured cells in central zone (CZ) and peripheral zone (PZ) shows no significant difference (Kolmogorov–Smirnov test, confidence level $\alpha = 0.05$, $D_{n,m} < D_\alpha$). (**v, w**) Normalized turgor pressure and co-aligned growth rate in subregions of SAM; $n$ is cell number, error bars indicate standard error of mean, lower case letters denote statistically significant groups (Student's $t$-test $p < 0.05$).
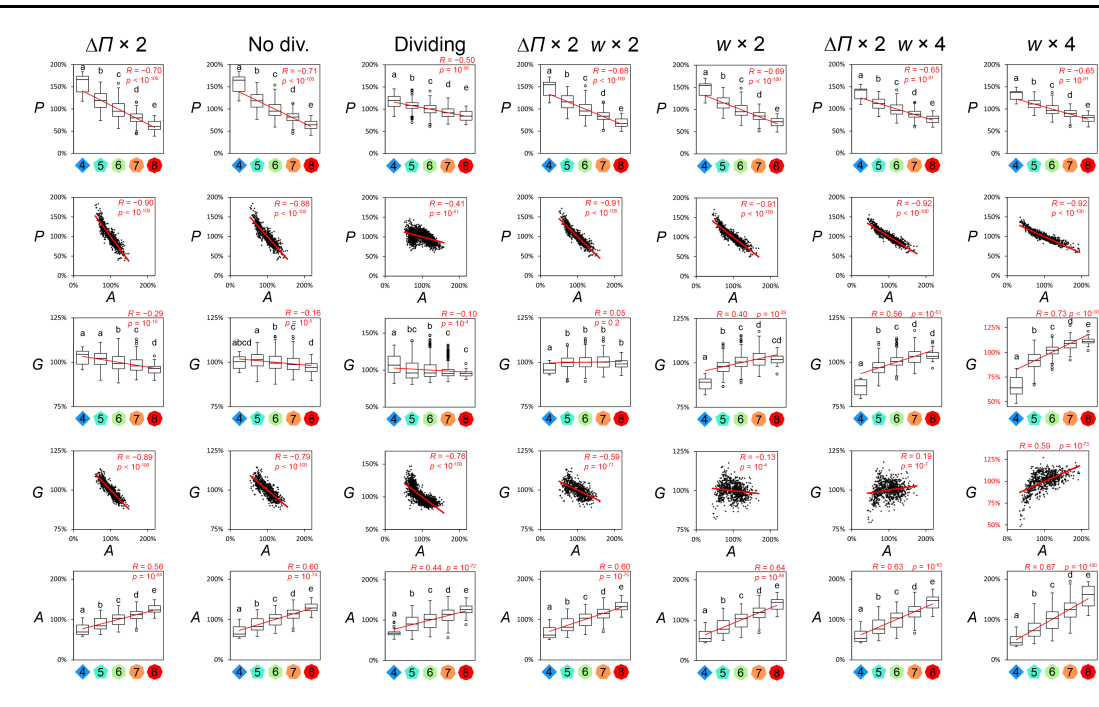


**Figure S6. Simulations to recapitulate oryzalin-treated SAM.**
Based on the reference parameter set ($\alpha^s = 0.5$, $\alpha^a = 0.5$, $\theta = 20/3$), which represents the untreated-like behaviour with cell divisions (Dividing), oryzalin-treated-like behaviour was further fitted by stopping cell division (No div.) and subsequently changing osmotic pressure $\Delta\Pi$ and cell wall thickness $w$, based on experimental observations. $P$, normalized turgor pressure, $A$, normalized cell area; $G$, normalized relative growth rate. Polygons indicate cell neighbour number. Red lines indicate linear regressions, with Pearson correlation coefficient $R$ and corresponding $p$-value.

757

758 **References**

759 1. Hong, L.; Dumond, M.; Zhu, M.; Tsugawa, S.; Li, C.-B.; Boudaoud, A.; Hamant, O.; Roeder,
760 A.H.K. Heterogeneity and Robustness in Plant Morphogenesis: From Cells to Organs. *Annu.*
761 *Rev. Plant Biol.* **2018**, *69*, 469–495.

762 2. Kamimoto, K.; Kaneko, K.; Kok, C.Y.-Y.; Okada, H.; Miyajima, A.; Itoh, T. Heterogeneity and
763 stochastic growth regulation of biliary epithelial cells dictate dynamic epithelial tissue
764 remodeling. *eLife* **2016**, *5*.

765 3. Ietswaart, R.; Rosa, S.; Wu, Z.; Dean, C.; Howard, M. Cell-Size-Dependent Transcription of FLC
766 and Its Antisense Long Non-coding RNA COOLAIR Explain Cell-to-Cell Expression Variation.
767 *Cell Syst.* **2017**, *4*, 622-635.e9.

768 4. Long, Y.; Stahl, Y.; Weidtkamp-Peters, S.; Postma, M.; Zhou, W.; Goedhart, J.; Sánchez-Pérez,
769 M.-I.; Gadella, T.W.J.; Simon, R.; Scheres, B.; et al. In vivo FRET-FLIM reveals cell-type-specific
770 protein interactions in Arabidopsis roots. *Nature* **2017**, *548*, 97–102.

771 5. Chubb, J.R. Symmetry breaking in development and stochastic gene expression. *Wiley*
772 *Interdiscip. Rev. Dev. Biol.* **2017**, *6*, e284.

773 6. Donati, G.; Watt, F.M. Stem Cell Heterogeneity and Plasticity in Epithelia. *Cell Stem Cell* **2015**,
774 *16*, 465–476.

775 7. Gerdes, M.J.; Sood, A.; Sevinsky, C.; Pris, A.D.; Zavodszky, M.I.; Ginty, F. Emerging
776 Understanding of Multiscale Tumor Heterogeneity. *Front. Oncol.* **2014**, *4*.

777 8. Eldar, A.; Elowitz, M.B. Functional roles for noise in genetic circuits. *Nature* **2010**, *467*, 167–
778 173.

779 9. Watanabe, K.; Umeda, T.; Niwa, K.; Naguro, I.; Ichijo, H. A PP6-ASK3 Module Coordinates the
780 Bidirectional Cell Volume Regulation under Osmotic Stress. *Cell Rep.* **2018**, *22*, 2809–2817.

781 10. Xie, K.; Yang, Y.; Jiang, H. Controlling Cellular Volume via Mechanical and Physical Properties
782 of Substrate. *Biophys. J.* **2018**, *114*, 675–687.

783 11. Guo, M.; Pegoraro, A.F.; Mao, A.; Zhou, E.H.; Arany, P.R.; Han, Y.; Burnette, D.T.; Jensen, M.H.;
784 Kasza, K.E.; Moore, J.R.; et al. Cell volume change through water efflux impacts cell stiffness
785 and stem cell fate. *Proc. Natl. Acad. Sci.* **2017**, *114*, E8618–E8627.

786 12. Dumais, J.; Forterre, Y. "Vegetable Dynamicks": The Role of Water in Plant Movements. *Annu.*
787 *Rev. Fluid Mech.* **2012**, *44*, 453–478.

788 13. Stewart, M.P.; Helenius, J.; Toyoda, Y.; Ramanathan, S.P.; Muller, D.J.; Hyman, A.A. Hydrostatic
789 pressure and the actomyosin cortex drive mitotic cell rounding. *Nature* **2011**, *469*, 226–230.

790 14. Montel, F.; Delarue, M.; Elgeti, J.; Malaquin, L.; Basan, M.; Risler, T.; Cabane, B.; Vignjevic, D.;
791 Prost, J.; Cappello, G.; et al. Stress clamp experiments on multicellular tumor spheroids. *Phys.*
792 *Rev. Lett.* **2011**, *107*, 188102.

793 15. Rojas, E.R.; Huang, K.C. Regulation of microbial growth by turgor pressure. *Curr. Opin.*
794 *Microbiol.* **2017**, *42*, 62–70.

795 16. Zerzour, R.; Kroeger, J.; Geitmann, A. Polar growth in pollen tubes is associated with spatially
796 confined dynamic changes in cell mechanical properties. *Dev. Biol.* **2009**, *334*, 437–446.

797 17. Lopez, R.; Badel, E.; Peraudeau, S.; Leblanc-Fournier, N.; Beaujard, F.; Julien, J.-L.; Cochard,
798 H.; Moulia, B. Tree shoot bending generates hydraulic pressure pulses: a new long-distance
799 signal? *J. Exp. Bot.* **2014**, *65*, 1997–2008.

800 18. Beauzamy, L.; Nakayama, N.; Boudaoud, A. Flowers under pressure: ins and outs of turgor

801        regulation in development. *Ann. Bot.* **2014**, mcu187.

802   19.   Feng, W.; Lindner, H.; Robbins, N.E.; Dinneny, J.R. Growing Out of Stress: The Role of Cell- and
803        Organ-Scale Growth Control in Plant Water-Stress Responses. *Plant Cell* **2016**, *28*, 1769–1782.

804   20.   Ortega, J.K. Augmented growth equation for cell wall expansion. *Plant Physiol.* **1985**, *79*, 318–
805        320.

806   21.   Kroeger, J.H.; Zerzour, R.; Geitmann, A. Regulator or driving force? The role of turgor pressure
807        in oscillatory plant cell growth. *PloS One* **2011**, *6*, e18549.

808   22.   Sager, R.E.; Lee, J.-Y. Plasmodesmata at a glance. *J. Cell Sci.* **2018**, *131*, jcs209346.

809   23.   Willmer, C.M.; Sexton, R. Stomata and plasmodesmata. *Protoplasma* **1979**, *100*, 113–124.

810   24.   Wille, A.C.; Lucas, W.J. Ultrastructural and histochemical studies on guard cells. *Planta* **1984**,
811        *160*, 129–142.

812   25.   Ruan, Y.L.; Llewellyn, D.J.; Furbank, R.T. The control of single-celled cotton fiber elongation
813        by developmentally reversible gating of plasmodesmata and coordinated expression of
814        sucrose and K+ transporters and expansin. *Plant Cell* **2001**, *13*, 47–60.

815   26.   Rygol, J.; Pritchard, J.; Zhu, J.J.; Tomos, A.D.; Zimmermann, U. Transpiration Induces Radial
816        Turgor Pressure Gradients in Wheat and Maize Roots. *Plant Physiol.* **1993**, *103*, 493–500.

817   27.   Robbins, N.E.; Dinneny, J.R. Growth is required for perception of water availability to pattern
818        root branches in plants. *Proc. Natl. Acad. Sci.* **2018**, *115*, E822–E831.

819   28.   Corson, F.; Hamant, O.; Bohn, S.; Traas, J.; Boudaoud, A.; Couder, Y. Turning a plant tissue into
820        a living cell froth through isotropic growth. *Proc. Natl. Acad. Sci. U. S. A.* **2009**, *106*, 8453–
821        8458.

822   29.   Ishihara, S.; Sugimura, K.; Cox, S.J.; Bonnet, I.; Bellaïche, Y.; Graner, F. Comparative study of
823        non-invasive force and stress inference methods in tissue. *Eur. Phys. J. E Soft Matter* **2013**,
824        *36*, 9859.

825   30.   Cheddadi, I.; Génard, M.; Bertin, N.; Godin, C. Coupling water fluxes with cell wall mechanics
826        in a multicellular model of plant development. *PLOS Comput. Biol.* **2019**, *15*, e1007121.

827   31.   Lucas, W.J.; Ham, B.-K.; Kim, J.-Y. Plasmodesmata - bridging the gap between neighboring
828        plant cells. *Trends Cell Biol.* **2009**, *19*, 495–503.

829   32.   Kumar, N.M.; Gilula, N.B. The Gap Junction Communication Channel. *Cell* **1996**, *84*, 381–388.

830   33.   McLean, P.F.; Cooley, L. Protein Equilibration through Somatic Ring Canals in Drosophila.
831        *Science* **2013**, *340*.

832   34.   Willis, L.; Refahi, Y.; Wightman, R.; Landrein, B.; Teles, J.; Huang, K.C.; Meyerowitz, E.M.;
833        Jönsson, H. Cell size and growth regulation in the Arabidopsis thaliana apical stem cell niche.
834        *Proc. Natl. Acad. Sci. U. S. A.* **2016**, *113*, E8238–E8246.

835   35.   Boyer, J.S.; Cavalieri, A.J.; Schulze, E.-D. Control of the rate of cell enlargement: Excision, wall
836        relaxation, and growth-induced water potentials. *Planta* **1985**, *163*, 527–543.

837   36.   Cosgrove, D.J. Cell Wall Yield Properties of Growing Tissue: Evaluation by in Vivo Stress
838        Relaxation. *Plant Physiol.* **1985**, *78*, 347–356.

839   37.   Ortega, J.K.E. Dimensionless Numbers to Analyze Expansive Growth Processes. *Plants* **2019**,
840        *8*, 17.

841   38.   Vella, D.; Ajdari, A.; Vaziri, A.; Boudaoud, A. The indentation of pressurized elastic shells: from
842        polymeric capsules to yeast cells. *J. R. Soc. Interface* **2012**, *9*, 448–455.

843   39.   Vella, D.; Ajdari, A.; Vaziri, A.; Boudaoud, A. Indentation of Ellipsoidal and Cylindrical Elastic
844        Shells. *Phys. Rev. Lett.* **2012**, *109*, 144302.

845  40.  Beauzamy, L.; Derr, J.; Boudaoud, A. Quantifying Hydrostatic Pressure in Plant Cells by Using
846       Indentation with an Atomic Force Microscope. *Biophys. J.* **2015**, *108*, 2448–2456.

847  41.  Beauzamy, L.; Louveaux, M.; Hamant, O.; Boudaoud, A. Mechanically, the Shoot Apical
848       Meristem of Arabidopsis Behaves like a Shell Inflated by a Pressure of About 1 MPa. *Front.*
849       *Plant Sci.* **2015**, *6*.

850  42.  Malgat, R.; Faure, F.; Boudaoud, A. A Mechanical Model to Interpret Cell-Scale Indentation
851       Experiments on Plant Tissues in Terms of Cell Wall Elasticity and Turgor Pressure. *Front. Plant*
852       *Sci.* **2016**, *7*.

853  43.  Lazarus, A.; Florijn, H.C.B.; Reis, P.M. Geometry-induced rigidity in nonspherical pressurized
854       elastic shells. *Phys. Rev. Lett.* **2012**, *109*, 144301.

855  44.  Kierzkowski, D.; Nakayama, N.; Routier-Kierzkowska, A.-L.; Weber, A.; Bayer, E.; Schorderet,
856       M.; Reinhardt, D.; Kuhlemeier, C.; Smith, R.S. Elastic domains regulate growth and
857       organogenesis in the plant shoot apical meristem. *Science* **2012**, *335*, 1096–1099.

858  45.  Milani, P.; Gholamirad, M.; Traas, J.; Arnéodo, A.; Boudaoud, A.; Argoul, F.; Hamant, O. In vivo
859       analysis of local wall stiffness at the shoot apical meristem in Arabidopsis using atomic force
860       microscopy. *Plant J. Cell Mol. Biol.* **2011**, *67*, 1116–1123.

861  46.  Mosca, G.; Sapala, A.; Strauss, S.; Routier-Kierzkowska, A.-L.; Smith, R.S. On the micro-
862       indentation of plant cells in a tissue context. *Phys. Biol.* **2017**, *14*, 015003.

863  47.  Hong, L.; Dumond, M.; Tsugawa, S.; Sapala, A.; Routier-Kierzkowska, A.-L.; Zhou, Y.; Chen, C.;
864       Kiss, A.; Zhu, M.; Hamant, O.; et al. Variable Cell Growth Yields Reproducible Organ
865       Development through Spatiotemporal Averaging. *Dev. Cell* **2016**, *38*, 15–32.

866  48.  Yi, H.; Chen, Y.; Wang, J.Z.; Puri, V.M.; Anderson, C.T. The stomatal flexoskeleton: how the
867       biomechanics of guard cell walls animate an elastic pressure vessel. *J. Exp. Bot.* **2019**, *70*,
868       3561–3572.

869  49.  Knoblauch, J.; Mullendore, D.L.; Jensen, K.H.; Knoblauch, M. Pico gauges for minimally
870       invasive intracellular hydrostatic pressure measurements. *Plant Physiol.* **2014**,
871       pp.114.245746.

872  50.  Nakayama, N.; Smith, R.S.; Mandel, T.; Robinson, S.; Kimura, S.; Boudaoud, A.; Kuhlemeier, C.
873       Mechanical Regulation of Auxin-Mediated Growth. *Curr. Biol.* **2012**, *22*, 1468–1476.

874  51.  Lewis, F.T. The correlation between cell division and the shapes and sizes of prismatic cells in
875       the epidermis of cucumis. *Anat. Rec.* **1928**, *38*, 341–376.

876  52.  Gibson, W.T.; Veldhuis, J.H.; Rubinstein, B.; Cartwright, H.N.; Perrimon, N.; Brodland, G.W.;
877       Nagpal, R.; Gibson, M.C. Control of the mitotic cleavage plane by local epithelial topology.
878       *Cell* **2011**, *144*, 427–438.

879  53.  Hamant, O.; Heisler, M.G.; Jönsson, H.; Krupinski, P.; Uyttewaal, M.; Bokov, P.; Corson, F.;
880       Sahlin, P.; Boudaoud, A.; Meyerowitz, E.M.; et al. Developmental Patterning by Mechanical
881       Signals in Arabidopsis. *Science* **2008**, *322*, 1650–1655.

882  54.  Kwiatkowska, D. Surface growth at the reproductive shoot apex of Arabidopsis thaliana pin-
883       formed 1 and wild type. *J. Exp. Bot.* **2004**, *55*, 1021–1032.

884  55.  Serrano-Mislata, A.; Schiessl, K.; Sablowski, R. Active Control of Cell Size Generates Spatial
885       Detail during Plant Organogenesis. *Curr. Biol.* **2015**, *25*, 2991–2996.

886  56.  Ali, O.; Mirabet, V.; Godin, C.; Traas, J. Physical models of plant development. *Annu. Rev. Cell*
887       *Dev. Biol.* **2014**, *30*, 59–78.

888  57.  Dumond, M.; Boudaoud, A. Physical Models of Plant Morphogenesis. In *Mathematical*

889       *Modelling in Plant Biology*; Morris, R.J., Ed.; Springer International Publishing: Cham, 2018;
890       pp. 1–14 ISBN 978-3-319-99070-5.

891   58.  Alt, S.; Ganguly, P.; Salbreux, G. Vertex models: from cell mechanics to tissue morphogenesis.
892       *Philos. Trans. R. Soc. B Biol. Sci.* **2017**, *372*.

893   59.  Dyson, R.J.; Vizcay-Barrena, G.; Band, L.R.; Fernandes, A.N.; French, A.P.; Fozard, J.A.;
894       Hodgman, T.C.; Kenobi, K.; Pridmore, T.P.; Stout, M.; et al. Mechanical modelling quantifies
895       the functional importance of outer tissue layers during root elongation and bending. *New*
896       *Phytol.* **2014**, *202*, 1212–1222.

897   60.  Forouzesh, E.; Goel, A.; Mackenzie, S.A.; Turner, J.A. In vivo extraction of Arabidopsis cell
898       turgor pressure using nanoindentation in conjunction with finite element modeling. *Plant J.*
899       **2013**, *73*, 509–520.

900   61.  Maurel, C.; Boursiac, Y.; Luu, D.-T.; Santoni, V.; Shahzad, Z.; Verdoucq, L. Aquaporins in Plants.
901       *Physiol. Rev.* **2015**, *95*, 1321–1358.

902   62.  Klepikova, A.V.; Kasianov, A.S.; Gerasimov, E.S.; Logacheva, M.D.; Penin, A.A. A high resolution
903       map of the Arabidopsis thaliana developmental transcriptome based on RNA-seq profiling.
904       *Plant J. Cell Mol. Biol.* **2016**, *88*, 1058–1070.

905   63.  Péret, B.; Li, G.; Zhao, J.; Band, L.R.; Voß, U.; Postaire, O.; Luu, D.-T.; Da Ines, O.; Casimiro, I.;
906       Lucas, M.; et al. Auxin regulates aquaporin function to facilitate lateral root emergence. *Nat.*
907       *Cell Biol.* **2012**, *14*, 991–998.

908   64.  Tsugawa, S.; Hervieux, N.; Kierzkowski, D.; Routier-Kierzkowska, A.-L.; Sapala, A.; Hamant, O.;
909       Smith, R.S.; Roeder, A.H.K.; Boudaoud, A.; Li, C.-B. Clones of cells switch from reduction to
910       enhancement of size variability in Arabidopsis sepals. *Development* **2017**, *144*, 4398–4405.

911   65.  Sapala, A.; Runions, A.; Routier-Kierzkowska, A.-L.; Das Gupta, M.; Hong, L.; Hofhuis, H.;
912       Verger, S.; Mosca, G.; Li, C.-B.; Hay, A.; et al. Why plants make puzzle cells, and how their
913       shape emerges. *eLife* **2018**, *7*.

914   66.  LeGoff, L.; Rouault, H.; Lecuit, T. A global pattern of mechanical stress polarizes cell divisions
915       and cell shape in the growing Drosophila wing disc. *Development* **2013**, *140*, 4051–4059.

916   67.  Campinho, P.; Behrndt, M.; Ranft, J.; Risler, T.; Minc, N.; Heisenberg, C.-P. Tension-oriented
917       cell divisions limit anisotropic tissue tension in epithelial spreading during zebrafish epiboly.
918       *Nat. Cell Biol.* **2013**, *15*, 1405–1414.

919   68.  Mao, Y.; Tournier, A.L.; Hoppe, A.; Kester, L.; Thompson, B.J.; Tapon, N. Differential
920       proliferation rates generate patterns of mechanical tension that orient tissue growth. *EMBO*
921       *J.* **2013**, *32*, 2790–2803.

922   69.  Louveaux, M.; Julien, J.-D.; Mirabet, V.; Boudaoud, A.; Hamant, O. Cell division plane
923       orientation based on tensile stress in Arabidopsis thaliana. *Proc. Natl. Acad. Sci.* **2016**, *113*,
924       E4294–E4303.

925   70.  Gibson, W.T.; Gibson, M.C. Chapter 4 Cell Topology, Geometry, and Morphogenesis in
926       Proliferating Epithelia. In *Current Topics in Developmental Biology*; Current Topics in
927       Developmental Biology; Academic Press, 2009; Vol. 89, pp. 87–114.

928   71.  Long, Y.; Boudaoud, A. Emergence of robust patterns from local rules during plant
929       development. *Curr. Opin. Plant Biol.* **2018**, *47*, 127–137.

930   72.  Vargas-Garcia, C.A.; Ghusinga, K.R.; Singh, A. Cell size control and gene expression
931       homeostasis in single-cells. *Curr. Opin. Syst. Biol.* **2018**, *8*, 109–116.

932   73.  Cutler, S.R.; Ehrhardt, D.W.; Griffitts, J.S.; Somerville, C.R. Random GFP::cDNA fusions enable

933 visualization of subcellular structures in cells of Arabidopsis at a high frequency. *Proc. Natl.*
934 *Acad. Sci.* **2000**, *97*, 3718–3723.

935 74. Stanislas, T.; Hamant, O.; Traas, J. Chapter 11 - In-vivo analysis of morphogenesis in plants. In
936 *Methods in Cell Biology*; Lecuit, T., Ed.; Cell Polarity and Morphogenesis; Academic Press,
937 2017; Vol. 139, pp. 203–223.

938 75. Reuille, P.B. de; Bohn-Courseau, I.; Godin, C.; Traas, J. A protocol to analyse cellular dynamics
939 during plant development. *Plant J.* **2005**, *44*, 1045–1053.

940 76. Legland, D.; Arganda-Carreras, I.; Andrey, P. MorphoLibJ: integrated library and plugins for
941 mathematical morphology with ImageJ. *Bioinformatics* **2016**, *32*, 3532–3534.

942 77. Mirabet, V.; Dubrulle, N.; Rambaud, L.; Beauzamy, L.; Dumond, M.; Long, Y.; Milani, P.;
943 Boudaoud, A. NanoIndentation, an ImageJ Plugin for the Quantification of Cell Mechanics.
944 *Methods Mol. Biol.* **in press**.

945 78. Sassi, M.; Ali, O.; Boudon, F.; Cloarec, G.; Abad, U.; Cellier, C.; Chen, X.; Gilles, B.; Milani, P.;
946 Friml, J.; et al. An auxin-mediated shift toward growth isotropy promotes organ formation at
947 the shoot meristem in Arabidopsis. *Curr. Biol. CB* **2014**, *24*, 2335–2342.

948 79. Kremer, A.; Lippens, S.; Bartunkova, S.; Asselbergh, B.; Blanpain, C.; Fendrych, M.; Goossens,
949 A.; Holt, M.; Janssens, S.; Krols, M.; et al. Developing 3D SEM in a broad biological context. *J.*
950 *Microsc.* **2015**, *259*, 80–96.

951 80. Kiss, A.; Moreau, T.; Mirabet, V.; Calugaru, C.I.; Boudaoud, A.; Das, P. Segmentation of 3D
952 images of plant tissues at multiple scales using the level set method. *Plant Methods* **2017**,
953 *13*, 114.

954 81. Reuille, P.B. de; Routier-Kierzkowska, A.-L.; Kierzkowski, D.; Bassel, G.W.; Schüpbach, T.;
955 Tauriello, G.; Bajpai, N.; Strauss, S.; Weber, A.; Kiss, A.; et al. MorphoGraphX: A platform for
956 quantifying morphogenesis in 4D. *eLife* **2015**, *4*, e05864.

957 82. Schmidt, T.; Pasternak, T.; Liu, K.; Blein, T.; Aubry-Hivet, D.; Dovzhenko, A.; Duerr, J.; Teale, W.;
958 Ditengou, F.A.; Burkhardt, H.; et al. The iRoCS Toolbox – 3D analysis of the plant root apical
959 meristem at cellular resolution. *Plant J.* **2014**, *77*, 806–814.

960